

Access to this work was provided by the University of Maryland, Baltimore County (UMBC) ScholarWorks@UMBC digital repository on the Maryland Shared Open Access (MD-SOAR) platform.

**Please provide feedback**

Please support the ScholarWorks@UMBC repository by emailing [scholarworks-group@umbc.edu](mailto:scholarworks-group@umbc.edu) and telling us what having access to this work means to you and why it's important to you. Thank you.



# SGR A\* AND ITS ENVIRONMENT: LOW-MASS STAR FORMATION, THE ORIGIN OF X-RAY GAS AND COLLIMATED OUTFLOW

F. YUSEF-ZADEH<sup>1</sup>, M. WARDLE<sup>2</sup>, R. SCHÖDEL<sup>3</sup>, D. A. ROBERTS<sup>1</sup>, W. COTTON<sup>4</sup>, H. BUSHOUSE<sup>5</sup>, R. ARENDT<sup>6</sup>, AND M. ROYSTER<sup>1</sup>

<sup>1</sup>CIERA, Department of Physics and Astronomy Northwestern University, Evanston, IL 60208, USA

<sup>2</sup>Department of Physics and Astronomy, Macquarie University, Sydney NSW 2109, Australia

<sup>3</sup>Instituto de Astrofísica de Andalucía (CSIC), Glorieta de la Astronomía, E-18008 Granada, Spain

<sup>4</sup>National Radio Astronomy Observatory, Charlottesville, VA 22903, USA

<sup>5</sup>Space Telescope Science Institute, 3700 San Martin Drive, Baltimore, MD 21218, USA

<sup>6</sup>NASA GSFC, Code 665, Greenbelt, MD 20771, USA

Received 2015 October 30; accepted 2015 December 16; published 2016 February 29

## ABSTRACT

We present high-resolution multiwavelength radio continuum images of the region within 150'' of Sgr A\*, revealing a number of new extended features and stellar sources in this region. First, we detect a continuous 2'' east–west ridge of radio emission, linking Sgr A\* and a cluster of stars associated with IRS 13 N and IRS 13E. The ridge suggests that an outflow of east–west blob-like structures is emerging from Sgr A\*. In particular, we find arc-like radio structures within the ridge with morphologies suggestive of photoevaporative protoplanetary disks. We use infrared K<sub>s</sub> and L' fluxes to show that the emission has similar characteristics to those of a protoplanetary disk irradiated by the intense radiation field at the Galactic center. This suggests that star formation has taken place within the S-cluster 2'' from Sgr A\*. We suggest that the diffuse X-ray emission associated with Sgr A\* is due to an expanding hot wind produced by the mass loss from B-type main sequence stars, and/or the disks of photoevaporation of low mass young stellar objects (YSOs) at a rate of  $\sim 10^{-6} M_{\odot} \text{ yr}^{-1}$ . The proposed model naturally reduces the inferred accretion rate and is an alternative to the inflow–outflow style models to explain the underluminous nature of Sgr A\*. Second, on a scale of 5'' from Sgr A\*, we detect new cometary radio and infrared sources at a position angle PA  $\sim 50^{\circ}$  which is similar to that of two other cometary sources X3 and X7, all of which face Sgr A\*. In addition, we detect a striking tower of radio emission at a PA  $\sim 50^{\circ}$ – $60^{\circ}$  along the major axis of the Sgr A East supernova remnant shell on a scale of 150'' from Sgr A\*. We suggest that the cometary sources and the tower feature are tracing interaction sites of a mildly relativistic jet from Sgr A\* with the atmosphere of stars and the nonthermal Sgr A East shell at a PA  $\sim 50^{\circ}$ – $60^{\circ}$  with  $\dot{M} \sim 1 \times 10^{-7} M_{\odot} \text{ yr}^{-1}$ , and opening angle  $10^{\circ}$ . Lastly, we suggest that the east–west ridge of radio emission traces an outflow that is potentially associated with past flaring activity from Sgr A\*. The position angle of the outflow driven by flaring activity is close to  $-90^{\circ}$ .

*Key words:* accretion, accretion disks – black hole physics – Galaxy: center

## 1. INTRODUCTION

A  $4 \times 10^6 M_{\odot}$  black hole is coincident with the compact nonthermal radio source Sgr A\* at the center of the Galaxy (Reid & Brunthaler 2004; Ghez et al. 2008; Gillessen et al. 2009). The estimated mass accretion rate onto Sgr A\* is several orders of magnitude smaller than the rate at which young, windy stars in the innermost 0.5 pc supply mass to the Bondi radius of Sgr A\* (Coker & Melia 1997; Cuadra et al. 2006, 2008). *Chandra* observations have characterized the X-ray emission surrounding Sgr A\* as being spatially extended with a radius of  $\sim 1''.5$  (Baganoff et al. 2003; Wang et al. 2013). The X-ray luminosity is interpreted as arising from a radiatively inefficient accretion flow (RIAF, e.g., Yuan et al. 2004). In this model, a fraction of the gaseous material accretes onto Sgr A\* and the rest is driven off as an outflow from Sgr A\* (e.g., Quataert 2004; Shcherbakov & Baganoff 2010; Wang et al. 2013). Another mechanism that may reduce the accretion rate is interaction with a jet or an outflow limiting the amount of gas falling onto Sgr A\* (Yusef-Zadeh et al. 2014a), thus modifying the accretion flow. In this picture, the interaction of the outflow with the surrounding gas or the atmosphere of mass-losing stars can provide an estimate of the power of the outflow.

Two different types of activity are associated with Sgr A\*. One is flaring on an hourly timescale at multiple wavelengths

(e.g., Baganoff et al. 2001; Genzel et al. 2003). Observations of Sgr A\* have detected a time delay at submillimeter, millimeter, and radio wavelengths consistent with a scenario in which plasma blobs expand away from the disk, becoming visible at successive longer wavelengths as the optical depths become of order unity effects (Yusef-Zadeh et al. 2006, 2008, 2009; Eckart et al. 2008; Marrone et al. 2008; Brinkerink et al. 2015). The other is a jet-driven outflow (e.g., Falcke & Markoff 2000). Unlike the flare activity, the existence of a jet from Sgr A\* has not been firmly established because of the complex thermal and nonthermal structures in this confused region of the Galaxy. At least five independent investigations based on X-ray, near-IR, and radio observations have suggested that a jet is emanating from Sgr A\*. These studies have found discrepant values for the jet position angle (PA) and inclination (Markoff et al. 2007; Munro et al. 2008; Broderick et al. 2011; Zamaninasab et al. 2011; Yusef-Zadeh et al. 2012; Li et al. 2013; Shahzamanian et al. 2015). It is possible that some of the gas approaching Sgr A\* is pushed away as part of an expanding hot plasma driven by flaring and jet activity, resulting in Sgr A\*'s low radiative efficiency. Thus, the presence of collimated structures from Sgr A\* is critical for distinguishing between the competing accretion and outflow models.

The Galactic center is a challenging region in which to image a radio jet or a flare close to Sgr A\*, because of the limited spatial resolution and dynamic range caused by confusing

**Table 1**  
VLA Observations of Sgr A\*

| Date        | Frequency<br>(GHz) | Bandwidth<br>(GHz) | Number of IFs | Number of Channels | $\theta_a \times \theta_b$ (PA)<br>(arcsec $\times$ arcsec) (degree) |
|-------------|--------------------|--------------------|---------------|--------------------|--|
| 2014 Feb 21 | 44.6               | 8                  | 16            | 64                 | $0.074 \times 0.034$ ( $-4.0$ )                                      |
| 2014 Mar 9  | 34.5               | 8                  | 16            | 64                 | $0.089 \times 0.046$ ( $-1.6$ )                                      |
| 2014 Mar 10 | 14.1               | 8                  | 16            | 64                 | $0.187 \times 0.073$ (0.6)   |
| 2014 Apr 17 | 8.9                | 2                  | 16            | 64                 | $0.187 \times 0.073$ (0.6)   |
| 2014 Apr 02 | 5.5                | 2                  | 16            | 64                 | $0.59 \times 0.27$ ( $-0.2$ )  |
| 2014 Apr 02 | 1.52               | 1                  | 16            | 64                 | $1.87 \times 0.91$ (0.8)   |

sources, scatter broadening, and intrinsic temporal variability of Sgr A\* on hourly timescales (e.g., Bower et al. 2014). Here we present sensitive observations of the Galactic center at multiple radio frequencies, obtained using the improved broadband capability of the Very Large Array (VLA), finding new radio structures interpreted to be associated with Sgr A\* activity.

On a scale of a few arcseconds from Sgr A\*, we identify a ridge of east–west radio emission which bends toward the SW in the direction away from Sgr A\*. This ridge, which is detected to the west of Sgr A\*, shows a number of blobs and arc-like features surrounded by a diffuse plume-like structure. We interpret the plume-like feature as arising from flaring activity, thus producing an outflow from the direction of Sgr A\* on a scale of  $\sim 0.1$  pc, with an opening angle of  $\sim 35^\circ$ . The PA of the outflow driven by flaring activity of Sgr A\* is consistent with the east–west elongation of Sgr A\* observed on a milliarcsecond (mas) scale (Bower et al. 2015). A large number of stars that are members of the so-called “S-cluster”<sup>7</sup> also lie along the ridge. We compare infrared and radio images of the ridge and argue that bow-shock structures detected within the inner  $2''$  of Sgr A\* are proplyd candidates. We show that radio sources with comparable scale sizes to those associated with proplyds cannot be simply blobs of dusty ionized gas but are associated with a reservoir of hot dust surrounded by ionized gas.

On a larger scale, within two arcminutes NE of Sgr A\*, we find new cometary sources (F1, F2, and F3) pointing toward Sgr A\* and a large-scale tower-like structure associated with the Sgr A East supernova remnant (SNR)  $150''$  from Sgr A\*. The PA of these new structures is similar to two other IR-identified cometary sources, X3 and X7, found to the SW of Sgr A\* (Mužić et al. 2007, 2010). One interpretation that we put forth is that these features could be the result of a jet from Sgr A\* interacting with the atmosphere of dusty stars near Sgr A\* and with the Sgr A East shell, respectively.

In addition, we suggest that the diffuse X-ray emission centered on Sgr A\* arises through hot gas created by the collision of stellar winds from B stars in the S-star cluster or young low-mass stars (c.f. Loeb 2004). This nuclear wind created by mass-losing stars near Sgr A\* produces hot expanding X-ray gas (c.f. Quataert 2004) that excludes the shocked winds from O and WR stars in the central parsec of the Galaxy and prevents accretion onto Sgr A\*. Meanwhile Sgr A\* accretes material from the cluster winds at a much lower rate, potentially explaining the low luminosity of Sgr A\* without the ejection of a large fraction of the accreted material.

<sup>7</sup> A loosely defined term consisting of  $\sim 30$  stars within a projected distance of  $1''$  from Sgr A\*,  $2/3$  of which are spectroscopically classified as O/B stars with orbital periods of a dozen to a few hundred years and the rest are older stars (e.g., Genzel et al. 2003). We point out that the stars in this region have different spectral types and ages and probably heterogeneous origins.

## 2. OBSERVATIONS AND DATA REDUCTION

### 2.1. Radio Data

Multi-wavelength radio continuum observations were carried out with the Karl G. Jansky VLA<sup>8</sup> in its A-configuration at 44, 34.5, 8.5, 5.5, and 1.4 GHz during 2014 March and April. Table 1 gives columns of the date, center frequency, bandwidth, the number of subbands (IF), the number of channels, and the spatial resolution of each observation. In all observations, we used 3C286 to calibrate the flux density scale, 3C286 and J1733-1304 (aka NRAO530) to calibrate the bandpass, and J1744-3116 to calibrate the complex gains. The broad 8 GHz bandwidths at 34 and 44 GHz, 2 GHz bandwidths at 5 and 14 GHz, and 1 GHz bandwidth at 1.4 GHz provide a significant improvement over earlier observations that had only 100 MHz of bandwidth. We observed Sgr A\* using the 3 bit sampler system at 34 and 44 GHz, which provided full polarization correlations.

### 2.2. Infrared Data

Details of the near-IR observations and data reduction of the Galactic center at the K<sub>s</sub> and L' bands, central wavelengths 2.18, and 3.8  $\mu\text{m}$ , respectively, were recently given in Yusef-Zadeh et al. (2015b). These observations used adaptive optics and were acquired with VLT/NACO,<sup>9</sup> with a pixel scale of  $0''.027$  per pixel. L'-band observations were obtained in speckle mode using five fields with different pointing and depths. Field 1 was centered on Sgr A\*, and Fields 2–5 were offset by approximately  $20''$  to the northeast, southeast, southwest, and northwest, respectively. Standard near-IR image data reduction was applied, followed by combining individual pointings into large mosaics. In the case of the L' image, the speckle holography technique, as described in Schödel et al. (2013), was applied to the thousands of obtained speckle frames to create final high-Strehl images for each pointing. Finally, we calibrated the images astrometrically by using the positions and proper motions of SiO maser stars in the Galactic center (Reid et al. 2007).

Imaging data in the M'-band were taken with NACO/VLT in 2003, 2004, and 2006. We retrieved the data from the ESO archive. Chopping was used for background subtraction. The images were flat-fielded and corrected for bad pixels. Since the chop throw was small in all observations (due to technical limitations at the VLT) the images from the individual epochs show strong negative residuals from stellar and diffuse sources in the off-target chop positions. However, some dithering was

<sup>8</sup> Karl G. Jansky Very Large Array (VLA) of the National Radio Astronomy Observatory is a facility of the National Science Foundation, operated under a cooperative agreement by Associated Universities, Inc.

<sup>9</sup> Based on observations made with ESO Telescopes at the La Silla or Paranal Observatories under programs ID 089.B-0503.

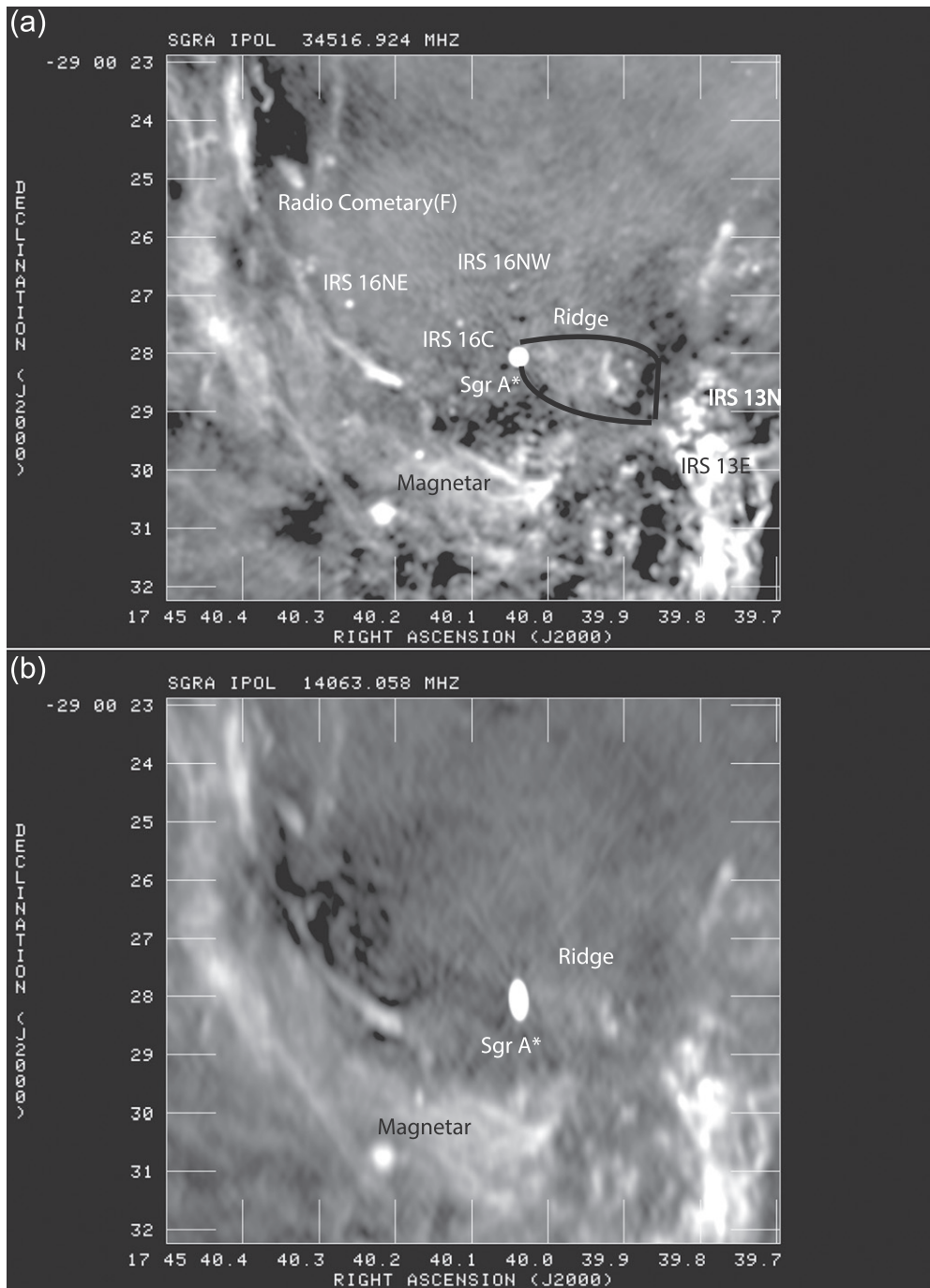


**Figure 1.** (a) A grayscale 34.5 GHz image convolved to a resolution of  $0''.1 \times 0''.1$  with grayscale range  $-0.3$  and  $1$  mJy. (b) The same as (a) except at the  $14.1$  GHz with a resolution of  $234 \times 108$  mas. (c) Similar to (a) except that the image display ranges between  $-0.31$  and  $0.1$  mJy. (d) Similar to (a) except in reverse color with a resolution  $88 \times 46$  mas.

applied during the observing runs and the initial pointing as well as the chopping angle were different for the different observing epochs. Therefore, residuals could be effectively removed by averaging the images from all observing epochs; the images were sub-pixel shifted onto a common position of the centroid of the star IRS 16C and median combined. Any remaining artifacts from chopping were effectively removed by rejecting the lowest 20% at each pixel before calculating the median value. Approximately 12,000 frames, each with a 0.056 s integration time, were combined, corresponding to an accumulated exposure time of about 800 s. The photometry

was calibrated by assuming constant extinction between the L and M bands and the same magnitudes at both bands for the sources IRS 16C and IRS 16NW. Their L'-band fluxes were taken from Schödel et al. (2010). The uncertainty of the zero point was estimated to be 0.15 mag.

### 3. RESULTS

Because of better sensitivity to detect weak radio emission, we first present newly recognized features within a few arcseconds of Sgr A\* and then compare the positions of near-IR

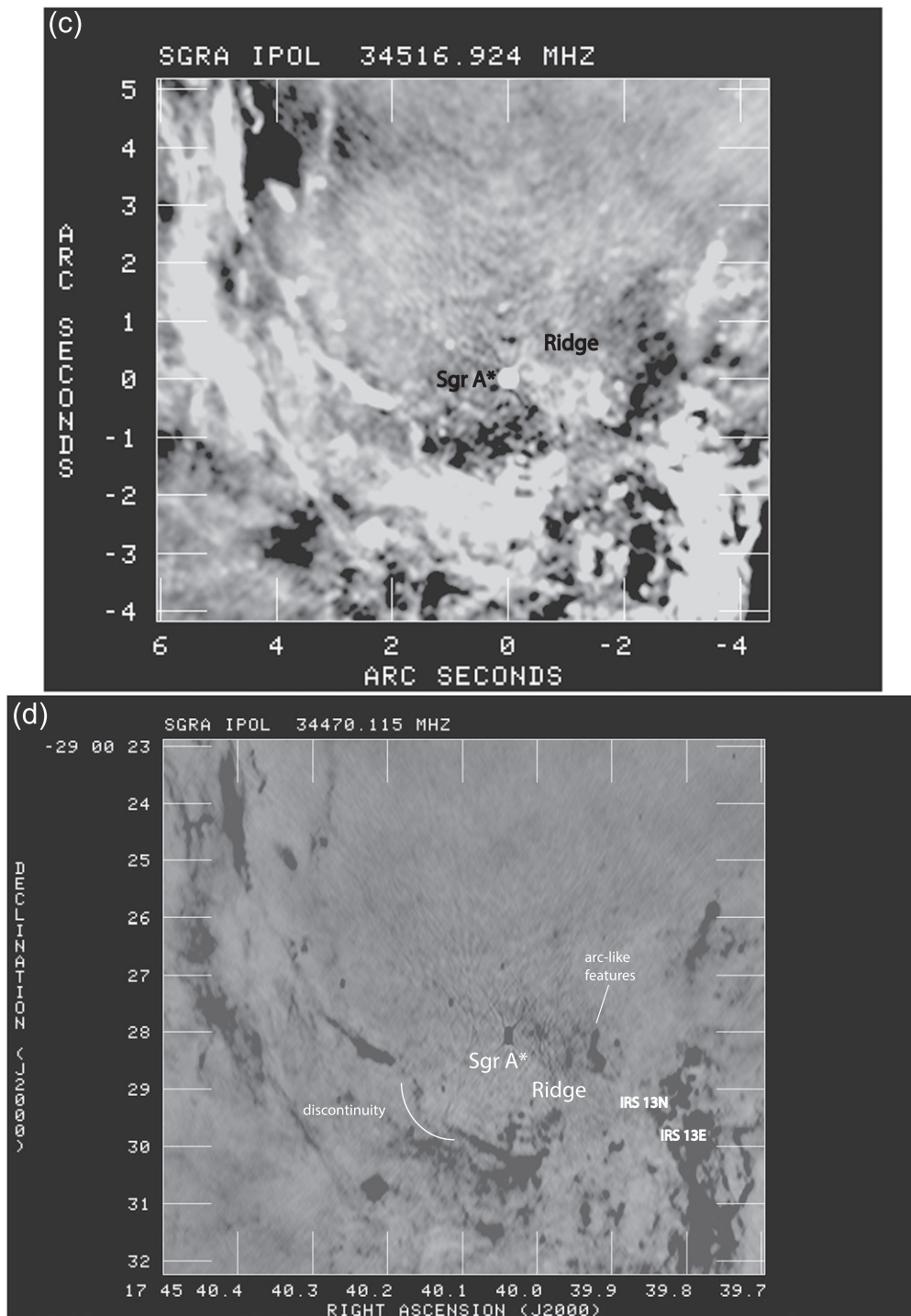


Figure 1. (Continued.)

identified stellar sources with radio data. Lastly, we present large structures on a scale between a few arcseconds to two arcminutes surrounding Sgr A\* and identify new features associated with the Sgr A East SNR shell.

### 3.1. Small Scale Radio Features

#### 3.1.1. The Sgr A\* Radio Ridge

Figures 1(a), (b) show images of the inner 10'' of Sgr A\* at mean frequencies (wavelengths) 34.5 GHz (9 mm) and

14.1 GHz (2 cm). Prominent stellar and ionized features are labeled. These images reveal a ridge of emission to the west of north of Sgr A\* extending for about 1''5–2'' at PAs ranging between  $\sim 90^\circ$  and  $-125^\circ$ . This ridge of emission, which was previously detected in low resolution images at 8 GHz (Wardle & Yusef-Zadeh 1992) links Sgr A\* to the western edge of the minicavity, an ionized feature with a diameter of 2''. The western edge of the minicavity coincides with the two stellar clusters IRS 13 N and IRS 13E. The Sgr A\* radio ridge consists of a number of blob-like and arc-like structures with angular

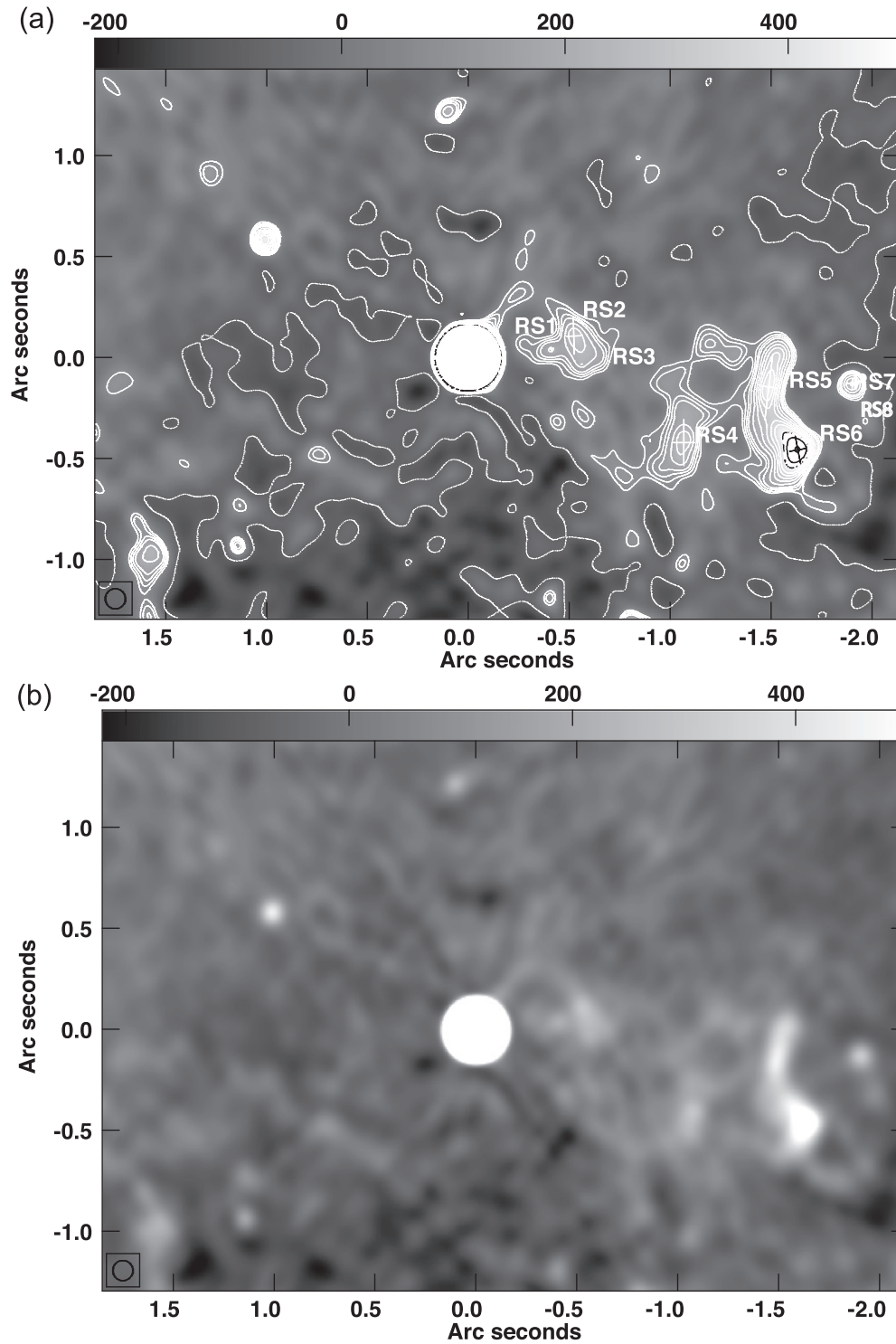


**Figure 2.** (a) A 34.5 GHz grayscale image similar to Figure 1(a) except that the image is convolved to a resolution of  $0''.1 \times 0''.1$ . The coordinate labels are given relative to the position of Sgr A\*. Eight radio sources are detected to the W of Sgr A\* in the east–west ridge within  $2''$  of Sgr A\* (see Table 5). The grayscale ranges between  $-220$  and  $500 \mu\text{Jy beam}^{-1}$ . (b) The same as (a) except no contours are drawn. (c) Similar to (a) except at 5.5 GHz with a resolution of  $0''.59 \times 0''.27$  (PA =  $-0^\circ.2$ ). The grayscale ranges between  $-2.5$  and  $5 \text{ mJy beam}^{-1}$ .

scales of  $0''.2$ – $0''.5$ . The two arc-like structures coincide with source  $\epsilon$ , which has been detected in earlier narrow bandwidth images with low spatial resolutions at 15 GHz (Yusef-Zadeh et al. 1990; Zhao et al. 1991). To illustrate the asymmetric nature of the ridge structure, Figure 1(c) shows a saturated image of the region shown in Figures 1(a), (b). We interpret this structure as having an opening angle of  $\sim 35^\circ$  pointed in the

direction toward W and SW from Sgr A\*. Figure 1(d) shows another 34.5 GHz rendition of the ridge of emission in reverse color, but at higher resolution than that of Figure 1(a). The images at multiple frequencies confirm the reality of blob and arc-like structures along the ridge. Note the diffuse plume-like structure, as drawn schematically on Figure 1(a), surrounding the blob and arc-like structures. The widening of the plume-like

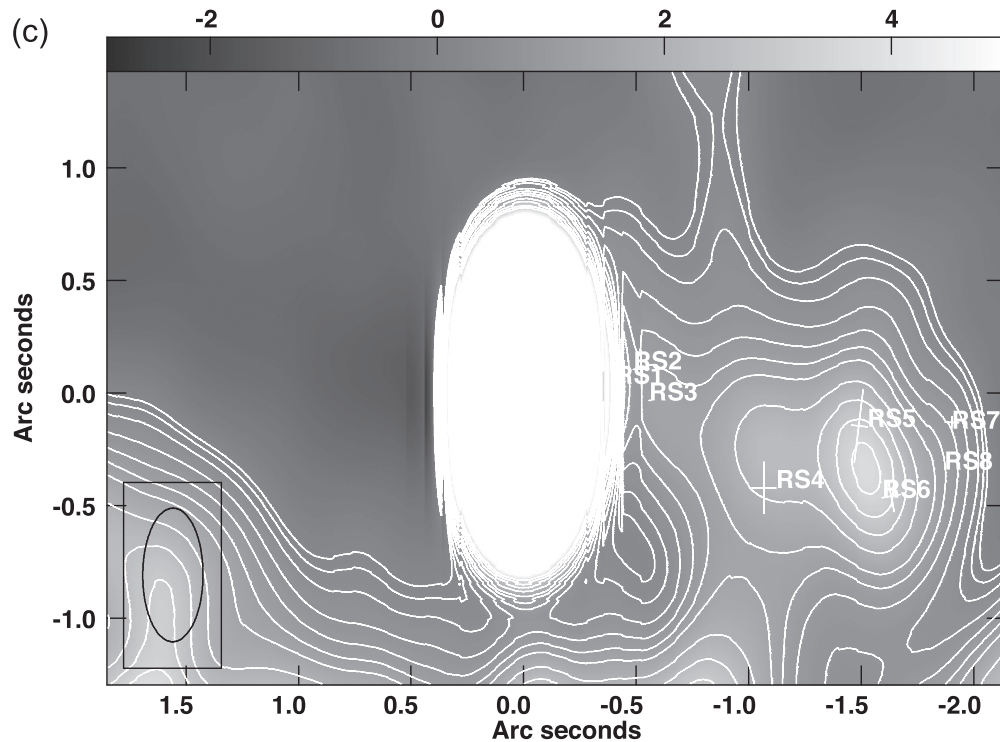


Figure 2. (Continued.)

Table 2

Predicted Positions of Young Stars in the S Cluster (Gillessen et al. 2009) at the 2014.19 Epoch

| Source Name | R.A. (IR)<br>17 <sup>h</sup> 45' | Decl. (IR)<br>−29°00' | ( $\sigma_x$ )<br>(arcsec) | ( $\sigma_y$ )<br>(arcsec) |
|-------------|----------------------------------|-----------------------|----------------------------|----------------------------|
| S1          | 40.0286                          | 28.1151               | 0.0144                     | 0.0187                     |
| S2          | 40.0411                          | 28.0174               | 0.0008                     | 0.0013                     |
| S4          | 40.0570                          | 28.0474               | 0.0216                     | 0.0086                     |
| S5          | 40.0348                          | 28.0605               | 0.0075                     | 0.0077                     |
| S6          | 40.0337                          | 28.0758               | 0.0212                     | 0.0024                     |
| S8          | 40.0793                          | 28.5629               | 0.0052                     | 0.0048                     |
| S9          | 40.0358                          | 28.0184               | 0.0058                     | 0.0090                     |
| S12         | 40.0490                          | 27.9601               | 0.0186                     | 0.0144                     |
| S13         | 40.0342                          | 28.3788               | 0.0221                     | 0.0156                     |
| S14         | 40.0529                          | 27.8995               | 0.0225                     | 0.0193                     |
| S17         | 40.0425                          | 27.7964               | 0.0015                     | 0.0060                     |
| S18         | 40.0414                          | 28.0197               | 0.0125                     | 0.0149                     |
| S19         | 40.0421                          | 28.1146               | 0.0203                     | 0.0077                     |
| S21         | 40.0417                          | 28.0590               | 0.0086                     | 0.0050                     |
| S24         | 40.0393                          | 28.1468               | 0.0031                     | 0.0166                     |
| S27         | 40.0397                          | 27.9761               | 0.0033                     | 0.0160                     |
| S29         | 40.0304                          | 27.9426               | 0.0866                     | 0.1822                     |
| S31         | 40.0387                          | 27.9182               | 0.0416                     | 0.1664                     |
| S33         | 39.9993                          | 28.1424               | 0.1097                     | 0.0620                     |
| S38         | 40.0404                          | 28.0739               | 0.0218                     | 0.0226                     |
| S66         | 39.9561                          | 27.8625               | 0.1121                     | 0.1450                     |
| S67         | 39.9990                          | 28.3748               | 0.0648                     | 0.0858                     |
| S71         | 40.0204                          | 28.2907               | 0.5941                     | 1.1285                     |
| S83         | 40.1387                          | 28.6212               | 0.9300                     | 0.1324                     |
| S87         | 39.9140                          | 28.3996               | 0.2083                     | 0.3649                     |
| S96         | 39.9402                          | 27.6973               | 0.1739                     | 0.2426                     |
| S97         | 40.0403                          | 29.0882               | 2.0261                     | 0.4675                     |

Table 3

Predicted Positions of S Stars (Lu et al. 2009) at the 2014.19 Epoch

| Source Name | R.A. (IR)<br>17 <sup>h</sup> 45' | Decl. (IR)<br>−29°00' | ( $\sigma_x$ )<br>(arcsec) | ( $\sigma_y$ )<br>(arcsec) |
|-------------|----------------------------------|-----------------------|----------------------------|----------------------------|
| S0-14       | 39.9808                          | 28.3463               | 0.0040                     | 0.0017                     |
| S0-15       | 39.9635                          | 27.9216               | 0.0039                     | 0.0016                     |
| S1-3        | 40.0587                          | 27.1722               | 0.0012                     | 0.0021                     |
| S1-2        | 40.0473                          | 29.0847               | 0.0017                     | 0.0063                     |
| S1-8        | 39.9958                          | 28.9944               | 0.0031                     | 0.0040                     |
| IRS16NW     | 40.0465                          | 26.8338               | 0.0009                     | 0.0033                     |
| IRS16C      | 40.1151                          | 27.4796               | 0.0023                     | 0.0012                     |
| S1-12       | 39.9839                          | 29.0952               | 0.0032                     | 0.0038                     |
| S1-14       | 39.9395                          | 28.456                | 0.0041                     | 0.0013                     |
| IRS16SW     | 40.1246                          | 29.0023               | 0.0025                     | 0.0023                     |
| S1-21       | 39.9143                          | 27.9777               | 0.0060                     | 0.0013                     |
| S1-22       | 39.9214                          | 28.5818               | 0.0049                     | 0.0018                     |
| S1-24       | 40.0941                          | 29.7428               | 0.0019                     | 0.0039                     |
| S2-4        | 40.1553                          | 29.5114               | 0.0036                     | 0.0036                     |
| IRS16CC     | 40.1886                          | 27.4463               | 0.0036                     | 0.0013                     |
| S2-6        | 40.1663                          | 29.3915               | 0.0027                     | 0.0023                     |
| S2-7        | 40.1074                          | 26.2056               | 0.0030                     | 0.0051                     |
| IRS29N      | 39.9219                          | 26.7034               | 0.0038                     | 0.0034                     |
| IRS16SWE    | 40.1835                          | 29.1707               | 0.0029                     | 0.0019                     |
| IRS33N      | 40.0362                          | 30.3219               | 0.0016                     | 0.0065                     |
| S2-17       | 40.1421                          | 29.9418               | 0.0033                     | 0.0047                     |
| S2-16       | 39.9546                          | 25.9938               | 0.0024                     | 0.0046                     |
| S2-19       | 40.0654                          | 25.7507               | 0.0015                     | 0.0047                     |
| S2-66       | 39.9283                          | 25.8824               | 0.0086                     | 0.0116                     |
| S2-74       | 40.0452                          | 25.2775               | 0.0020                     | 0.0063                     |
| IRS16NE     | 40.2596                          | 27.1622               | 0.0034                     | 0.0015                     |
| S3-5        | 40.2636                          | 29.2064               | 0.0049                     | 0.0022                     |
| IRS33E      | 40.0932                          | 31.1956               | 0.0054                     | 0.0107                     |
| S3-19       | 39.9227                          | 30.8233               | 0.0073                     | 0.0105                     |
| S3-25       | 40.1437                          | 25.1221               | 0.0055                     | 0.0089                     |
| S3-30       | 40.1623                          | 30.9647               | 0.0065                     | 0.0106                     |
| S3-10       | 40.2908                          | 29.1575               | 0.0060                     | 0.0026                     |

**Table 4**  
Predicted Positions of S Stars (Yelda et al. 2014) at the 2014.19 Epoch

| Source Name | R.A. (IR)<br>17 <sup>h</sup> 45' | Decl. (IR)<br>−29°00' | $dX$<br>(arcsec) | $dY$<br>(arcsec) |
|-------------|----------------------------------|-----------------------|------------------|------------------|
| S1-3        | 40.0586                          | 27.173                | 0.2669           | 0.8961           |
| S0-15       | 39.9637                          | 27.928                | −0.9786          | 0.1414           |
| IRS16C      | 40.1152                          | 27.479                | 1.0093           | 0.5898           |
| S1-12       | 39.9844                          | 29.099                | −0.7068          | −1.0301          |
| S1-14       | 39.9394                          | 28.465                | −1.2979          | −0.3955          |
| IRS16SW     | 40.1252                          | 28.999                | 1.1404           | −0.9304          |
| S0-14       | 39.9811                          | 28.352                | −0.7504          | −0.2828          |
| S1-1        | 40.1194                          | 28.022                | 1.0634           | 0.0475           |
| IRS16NW     | 40.0461                          | 28.838                | 0.1021           | 1.2310           |
| S1-33       | 39.9432                          | 28.042                | −1.2481          | 0.0273           |
| S1-18       | 39.9757                          | 26.554                | −0.8217          | 1.5152           |
| S1-22       | 39.9210                          | 28.595                | −1.5386          | −0.5256          |
| S2-4        | 40.1565                          | 29.508                | 1.5503           | −1.4388          |
| S2-7        | 40.1069                          | 26.204                | 0.9001           | 1.8649           |
| S2-6        | 40.1673                          | 29.386                | 1.6927           | −1.3167          |
| IRS16SW-E   | 40.184                           | 29.164                | 1.9187           | −1.0944          |
| S2-22       | 40.2131                          | 28.241                | 2.2934           | −0.1724          |
| S2-58       | 40.2015                          | 29.161                | 2.1414           | −1.0924          |
| S1-2        | 40.0482                          | 29.081                | 0.1296           | −1.0118          |
| S1-8        | 39.9966                          | 29.001                | −0.5473          | −0.9320          |
| S1-21       | 39.9145                          | 27.990                | −1.6247          | 0.0789           |
| S1-19       | 40.0738                          | 29.712                | 0.4655           | −1.6432          |
| S1-24       | 40.0951                          | 29.740                | 0.7451           | −1.6709          |
| IRS16CC     | 40.1888                          | 27.436                | 1.9748           | 0.6325           |
| IRS29N      | 39.9213                          | 26.7314               | −1.53534         | 1.3548           |
| IRS33N      | 40.0372                          | 30.3426               | −0.01349         | −2.2574          |
| S2-50       | 40.1686                          | 29.5458               | 1.70947          | −1.4895          |
| S2-17       | 40.1436                          | 29.9439               | 1.38141          | −1.8701          |
| S2-16       | 39.9538                          | 26.0307               | −1.10837         | 2.0622           |
| S2-21       | 39.9178                          | 29.7348               | −1.58133         | −1.6793          |
| S2-19       | 40.0646                          | 25.7450               | 0.34541          | 2.3194           |
| S2-74       | 40.0442                          | 25.2478               | 0.07746          | 2.7909           |
| S2-76       | 40.0220                          | 25.2451               | −0.21348         | 2.8184           |
| IRS16NE     | 40.2599                          | 27.1443               | 2.90649          | 0.9260           |
| S3-2        | 40.2748                          | 27.5406               | 3.10341          | 0.5632           |
| S3-3        | 40.2750                          | 28.6486               | 3.10449          | −0.6172          |
| S3-5        | 40.2648                          | 29.191                | 2.9708           | −1.1224          |
| S3-96       | 39.7994                          | 28.666                | −3.1334          | −0.5972          |
| S3-19       | 39.9227                          | 30.863                | −1.5164          | −2.7942          |
| IRS33E      | 40.0942                          | 31.203                | 0.7334           | −3.1336          |
| S3-25       | 40.1433                          | 25.105                | 1.3774           | 2.9641           |
| S3-26       | 39.8438                          | 30.125                | −2.5510          | −2.0555          |
| S3-30       | 40.1646                          | 30.979                | 1.6565           | −2.9103          |
| IRS13E1     | 39.8099                          | 29.729                | −2.9957          | −1.6596          |
| S3-190      | 39.7939                          | 26.660                | −3.2056          | 1.4093           |
| S3-10       | 40.2928                          | 29.148                | 3.3391           | −1.0790          |
| IRS13E4     | 39.7893                          | 29.462                | −3.2661          | −1.3927          |
| IRS13E2     | 39.7918                          | 29.786                | −3.2340          | −1.7167          |
| S3-314      | 40.3317                          | 28.133                | 3.8484           | −0.0639          |
| S3-331      | 39.9466                          | 24.390                | −1.2027          | 3.6787           |
| S3-374      | 39.8279                          | 30.929                | −2.7602          | −2.8595          |
| S4-36       | 39.7548                          | 26.300                | −3.7193          | 1.7690           |
| S4-71       | 40.0970                          | 32.171                | 0.7697           | −4.1025          |
| IRS34W      | 39.7271                          | 26.530                | −4.0827          | 1.5393           |
| S4-169      | 40.3739                          | 27.767                | 4.4024           | 0.3022           |
| IRS3E       | 39.8623                          | 24.245                | −2.3086          | 3.8236           |
| IRS7SE      | 40.2682                          | 24.599                | 3.0162           | 3.4705           |
| S4-258      | 39.7011                          | 29.683                | −4.4234          | −1.6136          |
| S4-262      | 40.3640                          | 30.039                | 4.2724           | −1.9700          |
| IRS34NW     | 39.7483                          | 25.252                | −3.8045          | 2.8174           |
| S4-287      | 40.0493                          | 32.826                | 0.1440           | −4.7570          |
| S4-364      | 40.2106                          | 23.603                | 2.2608           | 4.4663           |
| S5-34       | 39.7065                          | 30.811                | −4.3528          | −2.7421          |

**Table 4**  
(Continued)

| Source Name | R.A. (IR)<br>17 <sup>h</sup> 45' | Decl. (IR)<br>−29°00' | $dX$<br>(arcsec) | $dY$<br>(arcsec) |
|-------------|----------------------------------|-----------------------|------------------|------------------|
| IRS1W       | 40.4383                          | 27.392                | 5.2471           | 0.6768           |
| S5-235      | 40.2497                          | 23.540                | 2.7737           | 4.5289           |
| S5-237      | 40.4569                          | 27.026                | 5.4915           | 1.0431           |
| S5-236      | 39.6174                          | 29.340                | −5.5214          | −1.2707          |
| S5-183      | 40.3870                          | 31.513                | 4.5749           | −3.4439          |
| S5-187      | 39.9073                          | 33.626                | −1.7185          | −5.5571          |
| S5-231      | 40.4814                          | 27.937                | 5.8131           | 0.1319           |
| S5-191      | 40.2804                          | 32.963                | 3.1755           | −4.8942          |
| S6-89       | 40.4545                          | 25.086                | 5.4602           | 2.9830           |
| IRS9W       | 40.2609                          | 33.638                | 2.9201           | −5.5687          |
| S6-90       | 39.7367                          | 23.163                | −3.9571          | 4.9056           |
| S6-96       | 39.5767                          | 29.948                | −6.0548          | −1.8790          |
| S6-81       | 40.5221                          | 27.770                | 6.3469           | 0.2995           |
| S6-95       | 39.8557                          | 22.060                | −2.3955          | 6.0087           |
| S6-63       | 40.1824                          | 34.364                | 1.8900           | −6.2947          |
| S6-93       | 40.3795                          | 23.101                | 4.4765           | 4.9678           |
| S6-100      | 40.1551                          | 21.527                | 1.5319           | 6.5418           |
| S6-82       | 40.5512                          | 28.501                | 6.7288           | −0.4320          |
| S7-30       | 40.5303                          | 30.770                | 6.4538           | −2.7012          |
| S7-161      | 39.4753                          | 28.020                | −7.3861          | 0.0491           |
| S7-16       | 40.1630                          | 35.285                | 1.6362           | −7.2159          |
| S7-19       | 39.7511                          | 21.539                | −3.7671          | 6.5295           |
| S7-180      | 39.4757                          | 29.704                | −7.3807          | −1.6345          |
| S7-10       | 39.9517                          | 20.445                | −1.1363          | 7.6236           |
| S7-36       | 40.5245                          | 32.471                | 6.3780           | −4.4018          |
| S7-216      | 39.4498                          | 26.607                | −7.7205          | 1.4621           |
| S7-20       | 39.7581                          | 21.097                | −3.6762          | 6.9717           |
| S7-228      | 39.4492                          | 26.339                | −7.7281          | 1.7296           |
| S7-236      | 39.4958                          | 24.488                | −7.1167          | 3.5812           |
| S8-15       | 39.9146                          | 20.042                | −1.6228          | 8.0272           |
| S8-7        | 39.7592                          | 35.481                | −3.6613          | −7.4118          |
| S8-181      | 39.4564                          | 31.661                | −7.6335          | −3.5919          |
| S8-4        | 40.0363                          | 19.487                | −0.0264          | 8.5824           |
| S8-196      | 39.4219                          | 30.966                | −8.0861          | −2.8968          |
| S9-143      | 39.4005                          | 31.424                | −8.3670          | −3.3548          |
| S9-20       | 40.3676                          | 36.091                | 4.3203           | −8.0216          |
| S9-23       | 39.9392                          | 18.939                | −1.3003          | 9.1305           |
| S9-13       | 39.8091                          | 19.226                | −3.0070          | 8.8430           |
| S9-1        | 40.7579                          | 27.803                | 9.4396           | 0.2660           |
| S9-114      | 39.5431                          | 34.936                | −6.4968          | −6.8671          |
| S9-283      | 39.3065                          | 30.602                | −9.6001          | −2.5329          |
| S9-9        | 40.4686                          | 36.258                | 5.6447           | −8.1888          |
| S10-50      | 40.7688                          | 31.252                | 9.5831           | −3.1832          |
| S10-136     | 39.3801                          | 33.320                | −8.6351          | −5.2510          |
| S10-5       | 39.9176                          | 18.037                | −1.5838          | 10.0321          |
| S10-4       | 40.0433                          | 17.806                | 0.0653           | 10.2635          |
| S10-32      | 40.8174                          | 29.741                | 10.2201          | −1.6723          |
| S10-34      | 40.7155                          | 33.673                | 8.8832           | −5.6042          |
| S10-7       | 40.7783                          | 23.667                | 9.7069           | 4.4018           |
| S10-48      | 39.9987                          | 17.326                | −0.5190          | 10.7429          |
| S11-21      | 40.2329                          | 17.133                | 2.5531           | 10.9360          |
| S11-5       | 40.1426                          | 16.359                | 1.3684           | 11.7096          |
| S13-3       | 40.9456                          | 22.124                | 11.9027          | 5.9454           |

structure away from Sgr A\* suggests that a plume of gaseous material is moving outward and expanding away, suggesting that Sgr A\* is responsible for the ridge. Proper motion measurements of the brightest source in the ridge indicate high velocity ionized gas moving away from Sgr A\* to the SW (Zhao et al. 2009). This radio ridge appears distinct from the ionized gas associated with the mini-spiral H II region orbiting

**Table 5**  
Positions of Radio Sources

| ID  | Alt Name | R.A. (J2000)<br>(17 <sup>h</sup> 45 <sup>m</sup> ) | decl. (J2000)<br>(−29°00′) | Dist. from Sgr A*<br>(arcsec) | Pos. Accuracy<br>(mas) | $\theta_a \times \theta_b$ (PA)<br>(mas $\times$ mas) (degree) | Peak Intensity<br>(mJy beam <sup>−1</sup> ) | Integrated Flux<br>(mJy) |
|-----|----------|--|----------------------------|-------------------------------|------------------------|--|---|--------------------------|
| RS1 |          | 40.0070  | 28.0275                    | 0.41                          | 2.72                   | 21 $\times$ 0 (7)  | 0.178 $\pm$ 0.018                           | 0.133 $\pm$ 0.026        |
| RS2 |          | 39.9986  | 27.9628                    | 0.53                          | 5.94                   | 180 $\times$ 68 (1)  | 0.238 $\pm$ 0.017                           | 0.985 $\pm$ 0.084        |
| RS3 |          | 39.9955  | 28.1008                    | 0.56                          | 2.90                   | ...  | 0.197 $\pm$ 0.018                           | 0.102 $\pm$ 0.021        |
| RS4 |          | 39.9569  | 28.4896                    | 1.15                          | 8.27                   | 230 $\times$ 106 (180)   | 0.206 $\pm$ 0.016                           | 1.485 $\pm$ 0.133        |
| RS5 |          | 39.9248  | 28.2151                    | 1.50                          | 7.08                   | 326 $\times$ 76 (173)  | 0.329 $\pm$ 0.016                           | 2.492 $\pm$ 0.139        |
| RS6 |          | 39.9139  | 28.5265                    | 1.70                          | 2.46                   | 140 $\times$ 81 (11)   | 0.471 $\pm$ 0.017                           | 1.848 $\pm$ 0.080        |
| RS7 |          | 39.8933  | 28.1996                    | 1.91                          | 2.97                   | 59 $\times$ 53 (88)  | 0.254 $\pm$ 0.017                           | 0.492 $\pm$ 0.048        |
| RS8 |          | 39.8881  | 28.3757                    | 1.99                          | 8.58                   | 60 $\times$ 20 (14)  | 0.075 $\pm$ 0.014                           | 0.101 $\pm$ 0.030        |

Sgr A\* and is not confused with numerous dusty stellar sources and diffuse emission found in mid-IR images of this region. Future high resolution proper motion, polarization, and spectral index measurements of the ridge will provide additional constraints in the claim that this feature is associated physically to Sgr A\*.

### 3.1.2. Radio Emission from the S Cluster

The region within  $\sim 2''$  of Sgr A\* where the ridge of radio emission and the plume-like structure are detected, is adjacent to the S-cluster. This cluster consists mostly of young, early-type stars with orbital periods of 10 to a few 100 years. The kinematics of the stars in the cluster, which following other workers we refer to as “S stars,” have been used to measure the mass of Sgr A\* (Ghez et al. 2008; Gillessen et al. 2009). Figures 2(a), (b) show contours of 34.5 GHz emission and a grayscale image of a region of  $3''.5 \times 2''.5$  centered on Sgr A\*. Figure 2(c) shows contours of 5.5 GHz emission superimposed on a grayscale image. The crosses on Figures 2(a) and (c) correspond to eight radio sources RS1–8 found in the plume-like region to the west of Sgr A\*.

The trajectories of young stars are known from proper motion measurements in the near-IR. To see if these stars have radio continuum counterparts, their positions at the epoch of our 34 GHz observation on 2014 March 9 (2014.19) have been calculated based on proper motions and orbital accelerations have been derived from near-IR observations (Lu et al. 2009; Gillessen et al. 2009; Yelda et al. 2014). Tables 2 and 3 give the positions of the S-cluster and their corresponding positional uncertainties at the epoch of 2014.19 and from two different catalogs (Gillessen et al. 2006; Lu et al. 2009). Table 4 gives the predicted  $X/Y$  offsets (in arcsecond) of stars relative to Sgr A\* for the epoch 2014.19. These tables list the positions of the 28, 31, and 117 stars identified by Gillessen et al. (2009), Lu et al. (2009) and Yelda et al. 2014, respectively. Table 5 lists Gaussian-fitted positions of 8 radio sources (RS1–8) embedded within the diffuse extended emission associated with the Sgr A\* ridge and the plume-like structure at 34 GHz (see Figures 1 and 2). Entries in columns 1–9 give the name of the source at 34 GHz, alternative names in the literature, the R.A. and decl., the angular distance from Sgr A\* in increasing order, positional accuracy, the peak intensity, and the flux density that are associated with these sources.

Figures 3(a) and (b) superimpose contours of radio emission on a 34 GHz grayscale image, with crosses indicating the positions of the stars in the S-cluster for which orbits have been determined by Gillessen et al. (2009) and Lu et al. (2009),

respectively. Many of the S-stars, as noted in Figure 3(a), are projected against the bright, scatter-broadened radio source Sgr A\* and the diffuse emission from the Sgr A\* ridge, thus they cannot be discerned at radio wavelengths. The comparison of radio sources (RSs) listed in Table 5 with stellar sources given in Table 2 indicates that RS1, RS2, and RS3 lie within the  $1\sigma$  position of S33, which is an early-type star (Gillessen et al. 2009). These radio sources appear compact but they are embedded within the extended emission from the ridge of emission (see Figure 2(b)) so it is not clear if these sources are radio counterparts to S33 unless we measure the proper motion of radio sources. If these radio sources are not randomly coincident with S33 and are associated with stars, we can determine the mass loss rate from the ionized winds. The radio emission is assumed to arise from S33, with a flux density of  $\sim 0.2$  mJy at 34.5 GHz, and is due to a spherically symmetric, homogeneous wind of fully ionized gas expanding with a constant terminal velocity  $\sim 700$  km s<sup>−1</sup> (Panagia & Felli 1975). The mass loss rate of S33 is estimated to be  $\dot{M} = 2 \times 10^{-6} M_{\odot} \text{yr}^{-1}$ . Clumpiness of the ionized wind would reduce this estimate.

Figure 3(c) shows a grayscale 34 GHz image in negative and labeled with the positions of those stars for which orbits have been determined by Yelda et al. (2014). We note several prominent young stars, IRS 16SW, IRS 16NW, and IRS 16C, that are not members of the S-cluster but have radio counterparts (Yusef-Zadeh et al. 2014b). Figure 3(d) shows the distribution of stars over the area shown in Figure 3(c) at  $3.8 \mu\text{m}$ . The crosses correspond to the position of stars (Yelda et al. 2014) at the epoch that radio data were taken. Apart from stars labeled in this figure, the spectral classification of remaining faint sources is unknown. These faint sources are possibly late-type stars associated with the evolved nuclear cluster or young low-mass stars (see Section 4). Five near-IR stellar sources, A–E, are labeled on Figure 3(d) and will be discussed below.

### 3.1.3. Bow Shock-like Radio Sources RS5 and RS6

Figures 4(a), (b), (c) show the relative position of 34.5 GHz sources RS5–RS8 and  $3.8$  and  $2.18 \mu\text{m}$  sources A–D with respect to each other. Two of the newly detected radio sources in the ridge, RS5 and RS6, located  $\sim 1''.6$  from Sgr A\* (see Figure 2), are partially resolved, with size scales ranging between 850 and 1200 AU. Close-up views of these arc-like structures are shown in Figure 4(a), whereas Figures 4(b) and (c) show contours of  $3.8$  and  $2.18 \mu\text{m}$  emission superimposed on a 34.5 GHz image, respectively. A comparison of radio with

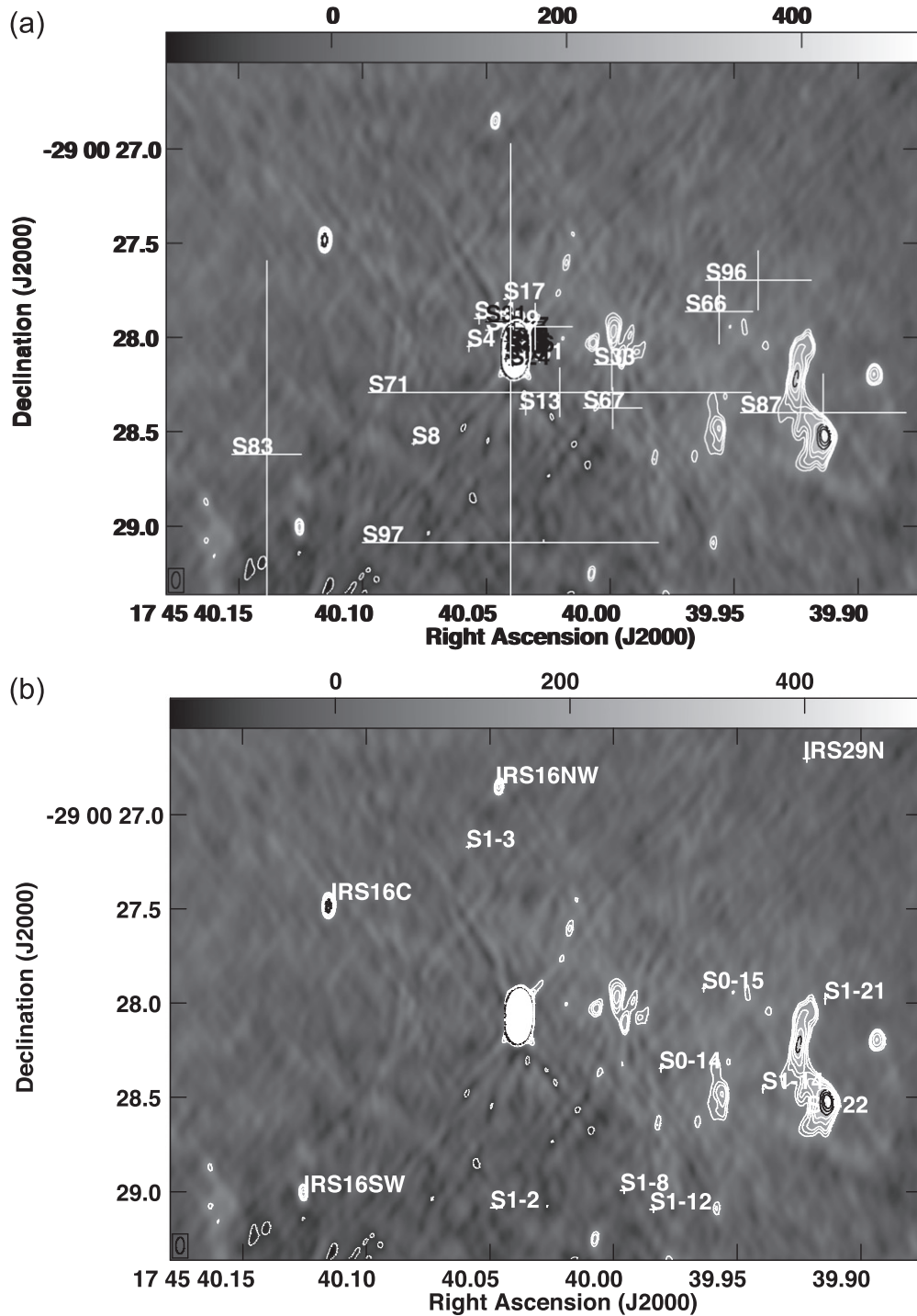


**Figure 3.** (a) Grayscale contours of 34.5 GHz emission at  $(-100, 100, 125, 150, 200, 250, \dots, 400) \times \mu\text{Jy beam}^{-1}$ . The error bars correspond to the predicted position of S-stars (Gillissen et al. 2009) at the epoch 2014.19. The resolution of the image is  $879 \times 448$  mas ( $\text{PA} = -2^\circ 5$ ). (b) Similar to (a) except that the crosses correspond to the position of stars given by Lu et al. (2009). The drawn error bars are twice the estimated values. The grayscale ranges between  $-140$  and  $500 \mu\text{Jy beam}^{-1}$  in both (a) and (b). (c) The same region as shown in (a) except that the image is convolved to a resolution of  $0''.1 \times 0''.1$ . The coordinate labels are given relative to the position of Sgr A\*. The crosses correspond to radio sources detected in the S-cluster RS1–8 (Table 4). The grayscale ranges between  $-200$  and  $500 \mu\text{Jy beam}^{-1}$ . (d) Similar to (c) except it is an  $L'$  image.

near-IR images reveals that the arc-like structures RS5 and RS6 have  $3.8 \mu\text{m}$  counterparts with a bow shock morphology. There are two near-IR stellar sources, S1-22 (Lu et al. 2009) and a stellar source A, as labeled in Figure 4(c). S1-22 lies at the apex of a bow shock-like structure and is an early-type star which is projected against the extended radio emission associated with

RS6. Star A has no radio counterpart, and is not identified in any catalogs of early-type stars near Sgr A\*. It is unlikely that star A is associated with RS6 for two reasons. First, proper motion measurements indicate that star A is moving to the NW with a velocity of  $117 \pm 16 \text{ km s}^{-1}$  (Schödel et al. 2009). The proper motion of ionized gas associated with the blob  $\epsilon$  which

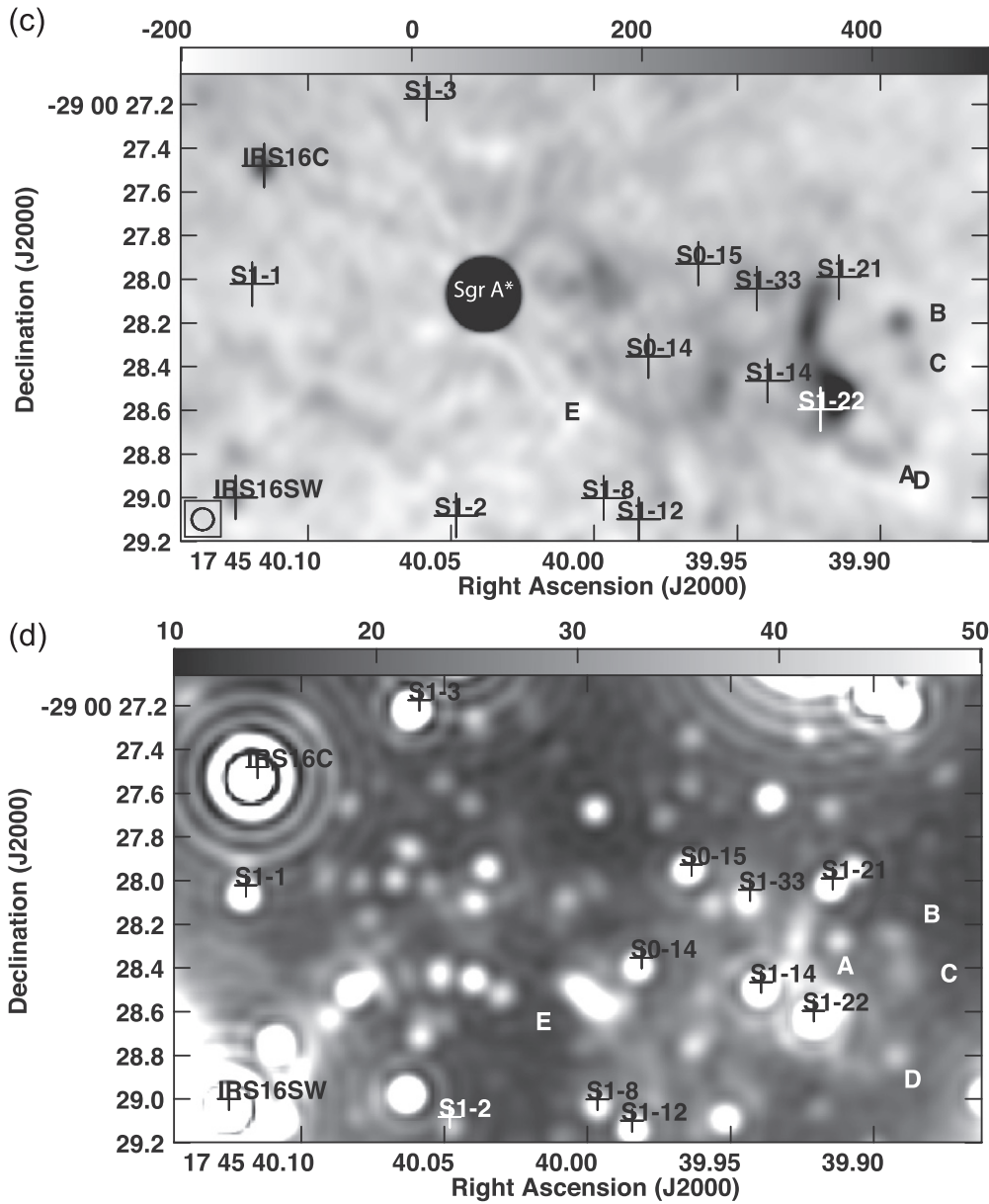
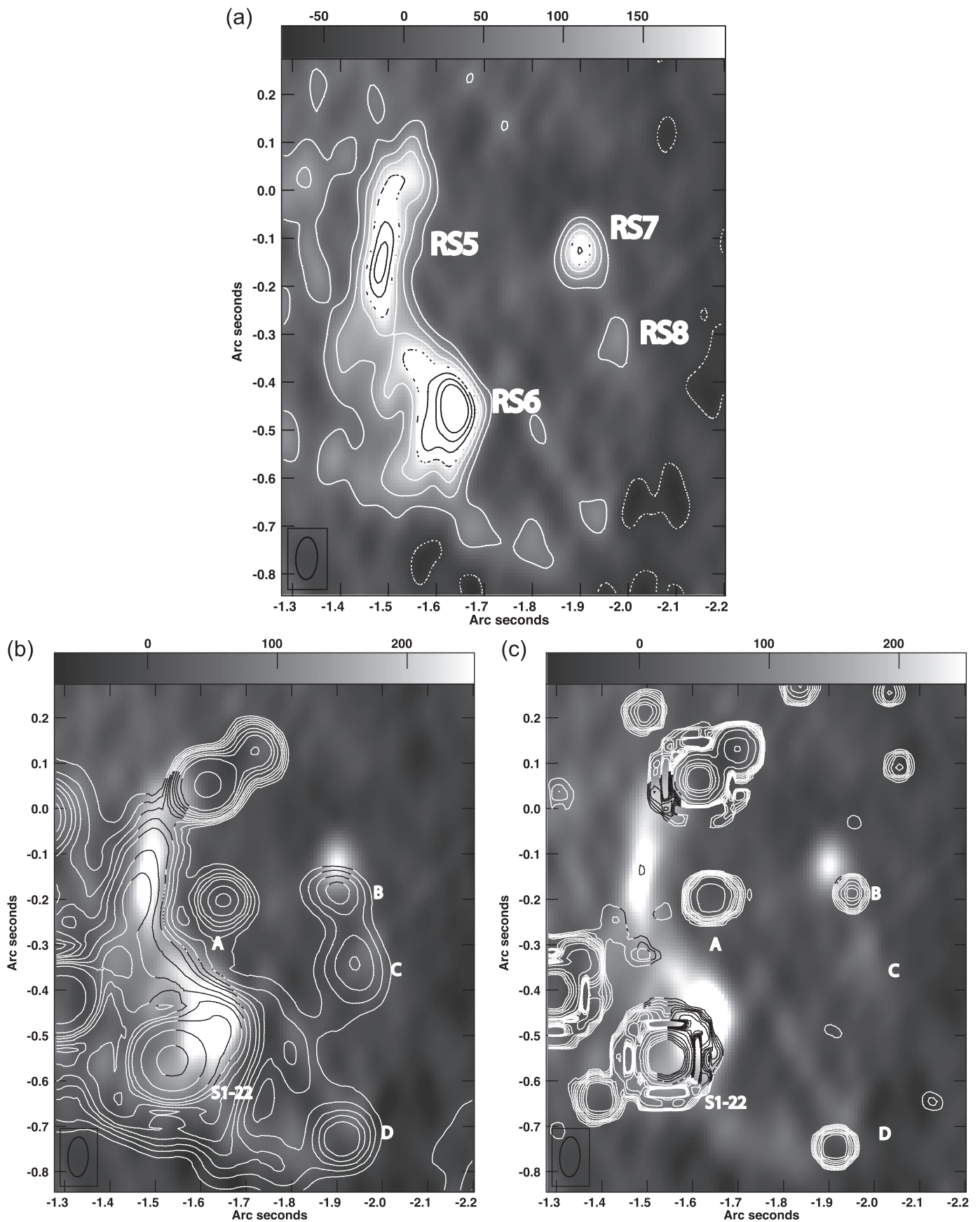


Figure 3. (Continued.)

coincides with RS5, RS6, and RS7 is  $\sim 338 \pm 21 \text{ km s}^{-1}$  to the SW (Zhao et al. 2009). Second, it is unlikely that a late-type star could have a stellar wind strong enough to produce the observed stand-off distance of the bow-shock’s apex,  $\sim 6$  milliparsec (mpc). This requires a Wolf–Rayet star (Tanner et al. 2005; Sanchez-Bermudez et al. 2014). Thus, it is unlikely that star A is associated with the bow-shock structure RS5.

As for S1-22, the proper motion data give a tangential velocity of  $\sim 326 \text{ km s}^{-1}$  to the SE (Yelda et al. 2014). Radio proper motion measurements have a coarse arcsecond spatial resolution, giving the proper motion of RS5, R6, and RS7, when compared to those of near-IR sources. In spite of the difference in resolution between radio and near-IR proper motion measurements, the magnitude of radio proper motion of RS5, RS6, and RS7 is similar to that of S1-22. Thus, it is possible that S1-22 is physically associated with RS6, with a standoff distance of  $\sim 4$  mpc.

In addition to star A, three  $3.8 \mu\text{m}$  sources B, C, and D, labeled in Figures 4(b) and (c), are not found in the catalogs of early-type stars. RS7 and RS8 are likely to be radio counterparts to sources B and C, respectively. A radio source with a flux density of  $58 \mu\text{Jy}$  at 34 GHz is detected at the position of source D that lies in an extended region associated with the ridge. The bright radio sources B and D are clearly stellar sources since they are detected at the  $L'$  and  $K_s$  bands. The offsets seen in the position of radio and near-IR sources could have a contribution from the proper motions of individual sources. The near-IR images at  $2.18$  and  $3.8 \mu\text{m}$  were taken during 2012 June and September whereas the 34.5 GHz data was taken on March 9, 2014. The  $L'$  sources associated with RS5, RS7 (or source A), RS8 (or source B), and D lie to the SSE of their radio counterparts, suggesting either correlated motion, coincidence, or a systematic error in the image registration arising because the radio and infrared images are



**Figure 4.** (a) Grayscale contours of 34.5 GHz emission at  $-50, 50, 100, 150, \dots, 350 \mu\text{Jy beam}^{-1}$  with a resolution of  $879 \times 448 \text{ mas}$  ( $\text{PA} = -2^\circ 5$ ). Radio sources are labeled. (b) The same area as in (a) except that contours of  $L'$  emission at  $2.5, 2.75, 3, 3.25, 3.5, 4, 4.5, 5, 6, 10, 20, 30, 40, 50 \times 10 \text{ mJy}$  are superimposed on a grayscale 34.5 GHz image. (c) The same as (b) except that contours of  $K_s$  emission with levels  $2.5, 2.75, 3, 3.25, 3.5, 4, 4.5, 5, 6, 10, 20, 30, 40, 50 \times 6.5 \text{ mJy}$  are superimposed on a grayscale 34.5 GHz image. The bar at the top shows the grayscale range in  $\mu\text{Jy}$ .

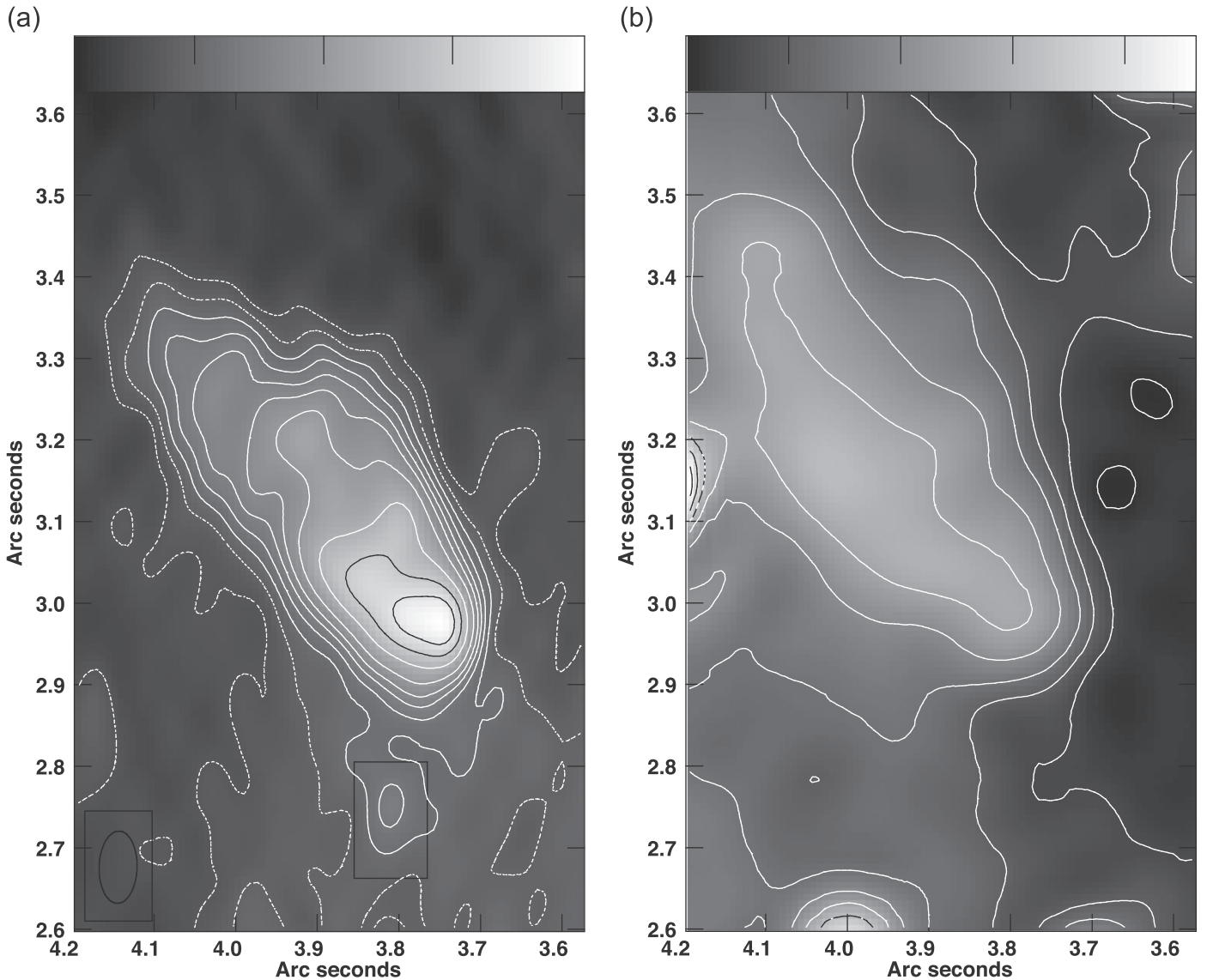


**Figure 5.** (a) Grayscale contours of 34.5 GHz emission from a cometary radio source (source F1) that points toward Sgr A\* at  $(-3, -1, 1, 3, 5, 7, 10, 15, 20, 25, 30) \times 10 \mu\text{Jy beam}^{-1}$ , with a resolution of  $879 \times 448 \text{ mas}$  ( $\text{PA} = -2.5^\circ$ ). The range in grayscale is between  $-100$  and  $300 \mu\text{mJy beam}^{-1}$ . (b) Similar to (a) except at  $3.8 \mu\text{m}$  with contour levels (16, 18, 20, 22, 25, 28, 34, 37)  $\text{mJy per } 27 \text{ mas}^2$ . The range in grayscale is between 15 and 38  $\text{mJy}$ . (c) An  $M'$  band grayscale image at  $4.68 \mu\text{m}$  in reverse color shows dusty stars and clouds near Sgr A\*. The inset to the right shows a blow-up of a rectangular region marked by dashed lines. Contour levels are set at 0.02, 0.04, 0.06, 0.08  $\text{Jy per arcsecond}^2$ . The labeled MIR cometary is also called source F2. (d) Grayscale contours of emission from the cometary source F3 at 34.5 GHz at  $(-6, 6, 10, 15, 18, 22, 30, 40, 50 \text{ and } 60 \mu\text{Jy beam}^{-1})$ . The grayscale range is between  $-40$  and  $200 \mu\text{Jy}$ .

taken at different epochs. We compared Gaussian fitted positions of B, C, and D at 34.5 GHz and the  $L'$  band and found 3.4 and 3 sigma offsets to the north in the positions of stars B and D and their radio counterparts, respectively. We also compared the positional offset for IRS 16C and its radio counterpart and determined that this implies a proper motion of IRS 16 that is roughly two times the actual value determined at radio and infrared wavelengths (Lu et al. 2009; Yusef-Zadeh et al. 2015a). Thus, we can not establish that radio sources are counterparts to stellar sources. Given the offsets in positions and the non-detection of source C in  $K_s$ , it is just possible that the radio sources are gas blobs and are not directly associated with stars. However, it is not clear how gas blobs near Sgr A\* could survive the tidal shear of Sgr A\* unless they have densities that withstand the tidal shear or they are transient (Yusef-Zadeh et al. 2015c).

### 3.2. Large Scale Features

#### 3.2.1. Cometary Sources F1 and F2

There are two known cometary sources, X3 and X7, lying within  $3''$  to the SW of Sgr A\* at near-IR wavelengths. X3 is located  $\sim 3''$  from Sgr A\* (Mužić et al. 2007, 2010), showing a tail-head structure pointing toward Sgr A\*. It has a radio counterpart at 44 GHz (source 16 in Yusef-Zadeh et al. 2014b) and a peak flux density of  $0.22 \text{ mJy beam}^{-1}$  at 34.5 GHz. The second cometary source X7 (Mužić et al. 2007) is identified in Figure 3(d) as source E at near-IR. This cometary source also points toward the direction of Sgr A\*. A compact 34.5 GHz source with a peak flux density of  $100 \mu\text{Jy}$  is detected at the position of source E  $0''.7$  from Sgr A\*. This source lies too close to Sgr A\*, where the noise increases near the bright source Sgr A\*, thus structural details of this source are not clear

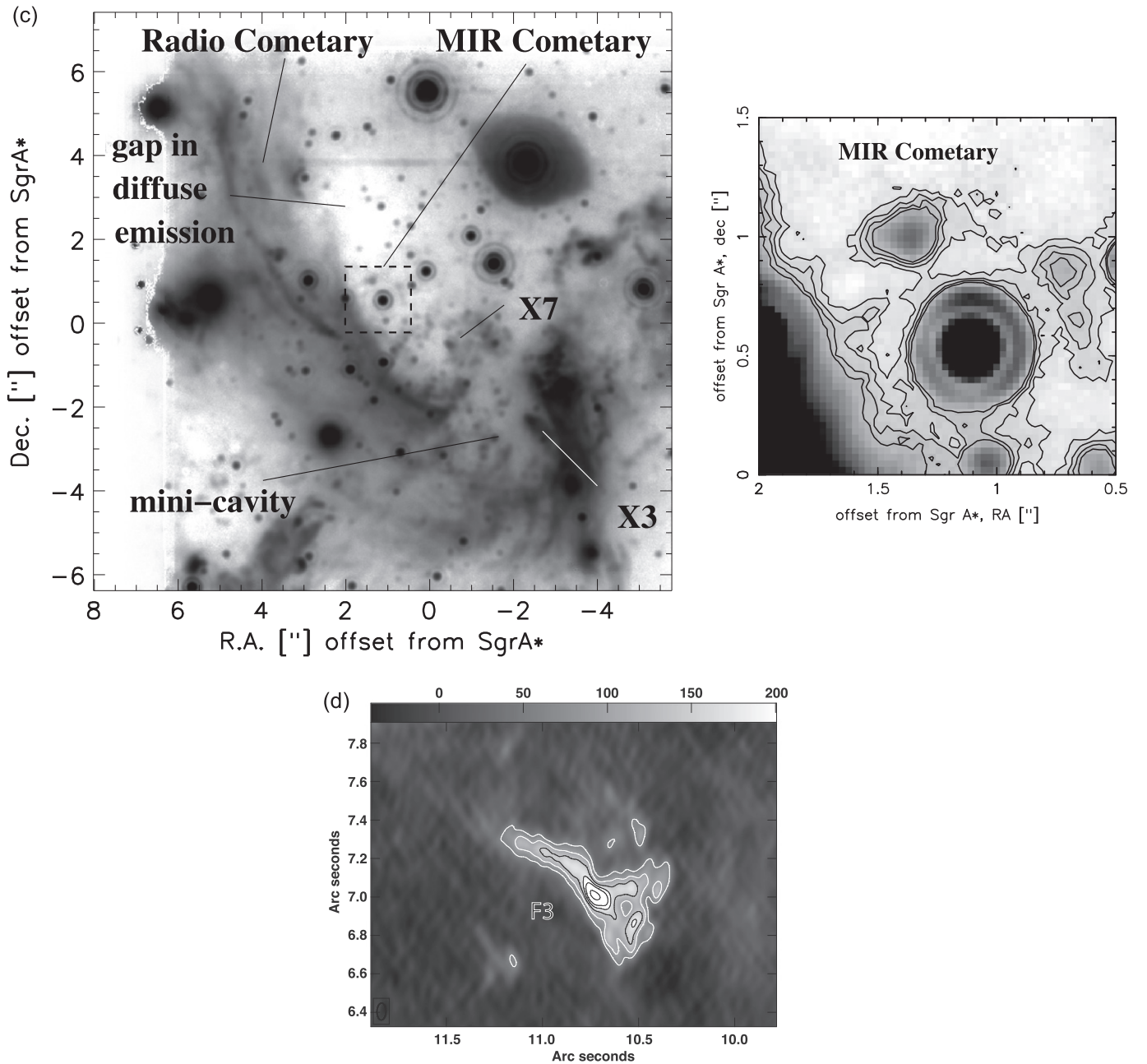


Figure 5. (Continued.)

at radio wavelengths. We detect a third radio source with a cometary morphology similar to X3 and X7. Unlike X3 and X7, this source, which we denote F1, lies  $4''.8$  to the NE of Sgr A\*. Figures 5(a), (b) show grayscale contours of this cometary feature at 34.5 GHz and  $3.8 \mu\text{m}$ , respectively. F1 has an extent of  $0''.65 \times 0''.25$  (length  $\times$  width) with an integrated flux density of  $\sim 2$  mJy and a background subtracted peak intensity of 416 mJy per  $(0''.12)^2$  at 34.5 GHz and  $3.8 \mu\text{m}$ , respectively.

Figure 5(c) shows a large view of the region which includes X3, X7, the radio cometary feature (F1), and the MIR cometary feature (F2) at  $4.68 \mu\text{m}$  in reverse color. We note a gap in the region to the NE of Sgr A\* where F1 is detected. This gap appears to be devoid of dust emission at MIR. The MIR gap

can also be identified at radio in Figure 1(b). However, the lack of short  $uv$  spacings may contribute in suppressing the emission from the bright source Sgr A\*. A close-up view of the infrared emission at the M' band from the inner  $3'' \times 3''$  of Sgr A\* is shown in the inset to the right of Figure 5(c). An additional cometary feature is detected at MIR to the NE of IRS 16C in the inset. This source, which we call F2, is well within the MIR gap and lies along the direction where X3, X7, and F1 are located.

Lastly, an additional radio source  $\sim 13''$  NE of Sgr A\* shows a head-tail structure pointing toward Sgr A\* (see Figure 5(d)). This radio feature shows a tail feature with an extent of  $\sim 0''.6$  at the PS  $\sim 57''$ . The peak flux density of this source, which we call F3, is  $0.32 \text{ mJy beam}^{-1}$  at 34.5 GHz with a spatial

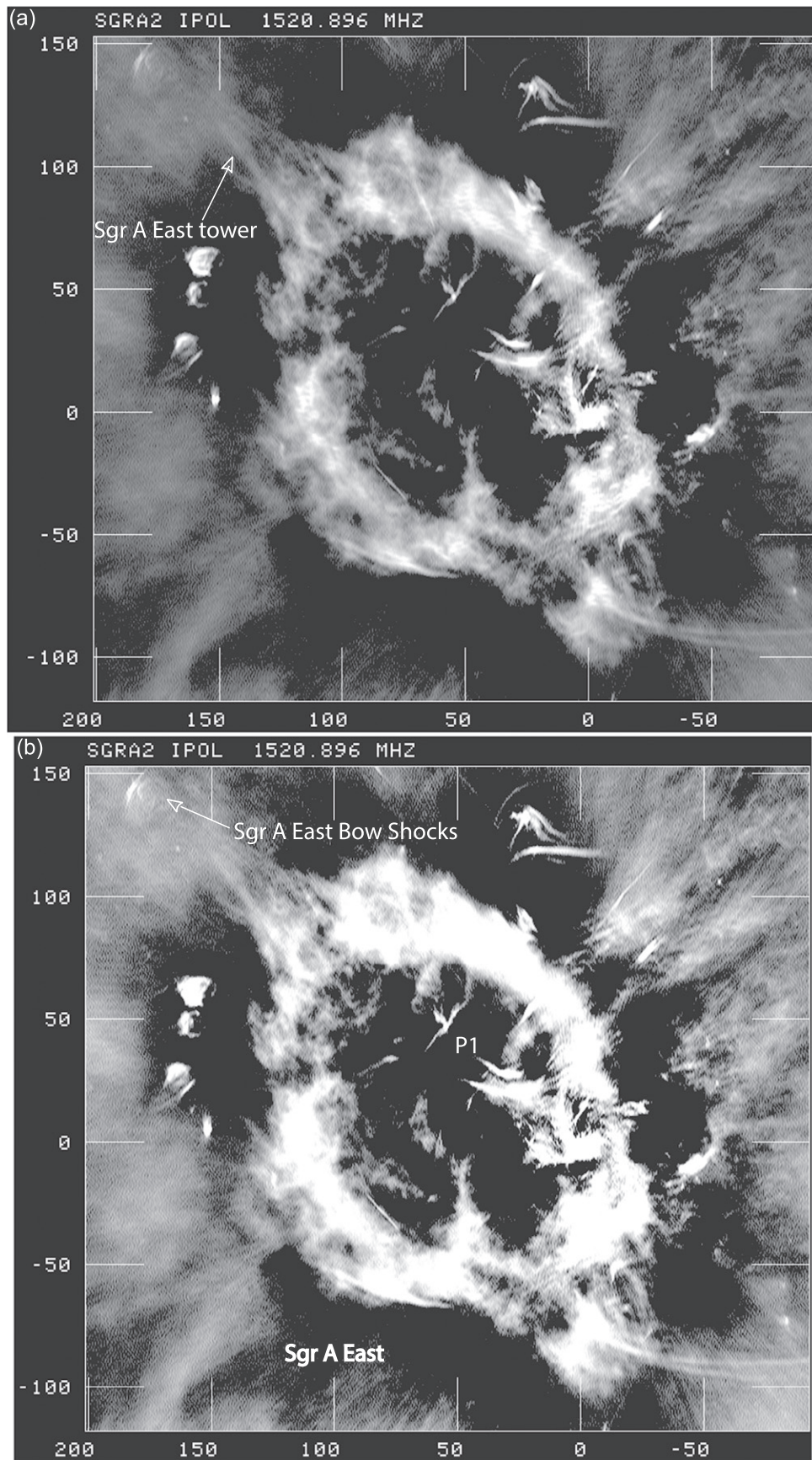


**Figure 6.** (a) A grayscale scale image of Sgr A East and West at 1.5 GHz with a resolution of  $1''.4 \times 0''.6$  ( $PA = -1^\circ$ ). The brightness range of the grayscale is between  $-1.5 \times 10^{-4}$  and  $0.002 \text{ Jy beam}^{-1}$ . (b) Similar to (a) except that the grayscale ranges are between  $-1.5 \times 10^{-4}$  and  $5 \times 10^{-4} \text{ Jy beam}^{-1}$ . The  $1\sigma$  rms noise is  $53 \mu\text{Jy beam}^{-1}$ . (c) A schematic diagram of features noted at 1.5 GHz.

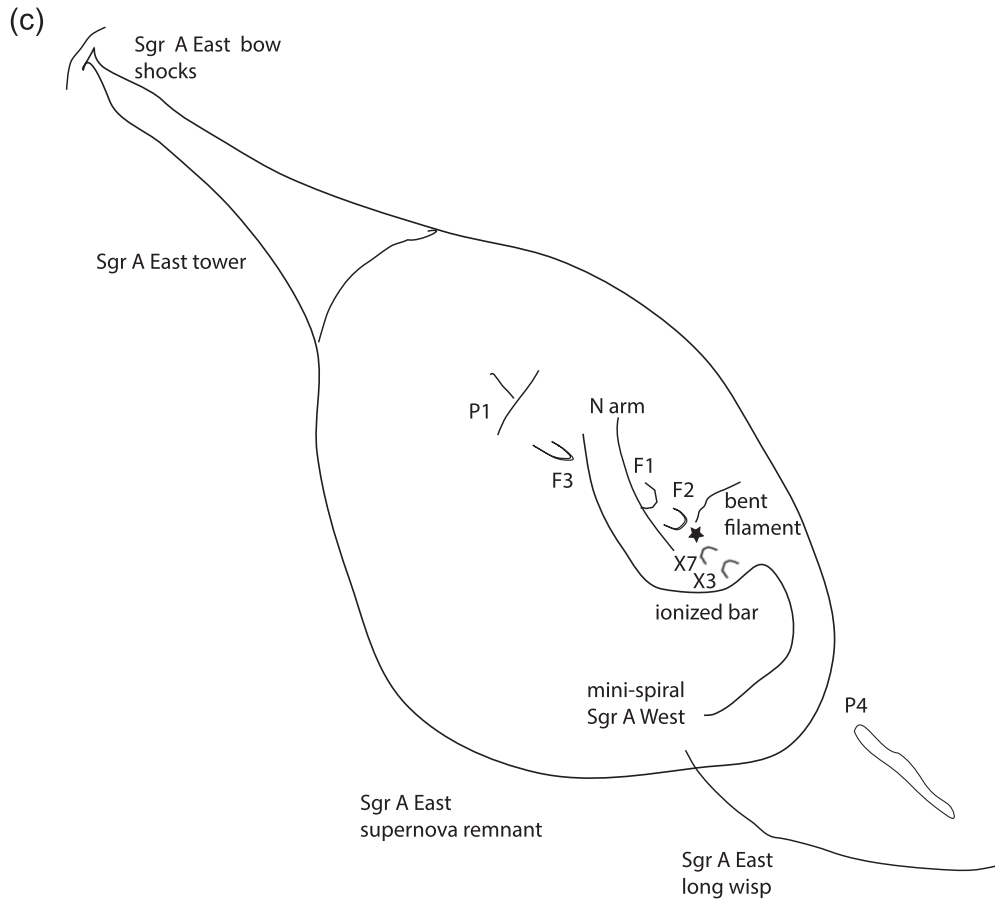


Figure 6. (Continued.)

resolution of  $89'' \times 46''$  mas. This source has been detected in the  $L'$  band as IRS 5 SE (Perger et al. 2008). This source is interpreted as a stellar bow-shock resulting from the interaction of mass-losing stars and the mini-spiral.

### 3.2.2. Sgr A East Tower

The nonthermal radio source Sgr A East is a young shell-type SNR with an angular size of  $2'.7 \times 3'.6$  and a spectral index  $\alpha = 0.76$ , where the flux density  $S_\nu \propto \nu^{-\alpha}$  (Ekers et al. 1983; Yusef-Zadeh & Morris 1987; Pedlar et al. 1989). Thermal X-ray emission is concentrated in the interior of the remnant, suggesting that Sgr A East is a mixed morphology SNR interacting with the  $50 \text{ km s}^{-1}$  molecular cloud (Maeda et al. 2002; Park et al. 2005). The thermal X-ray emitting plasma has two components, characterized by temperatures of 1 and 6 keV and corresponding electron density of 4.7 and  $0.6 \text{ cm}^{-3}$ , respectively. (Park et al. 2005; Koyama et al. 2007). A candidate neutron star CXOGC J174545.5–285829 (the cannonball) detected in X-ray and radio has also been associated with the remnant (Park et al. 2005; Zhao et al. 2013).

Our broad band 1.5 GHz image of Sgr A East provides a wealth of details associated with Sgr A East and the surrounding environment. Figures 6(a) and (b) show large scale views of Sgr A East displayed with two different grayscale levels at 1.5 GHz. The major axis of the Sgr A East shell is along the Galactic plane. A number of new features are detected in this complex region. Here we describe three new features. One is a distorted region to the NE of the Sgr A East

shell,  $100''$  E and  $80''$  N of Sgr A\*. A striking tower-like structure with an extent of  $100''$  appears to emerge from a gap in the brightness distribution of Sgr A East. The base of this tower is about  $20''$ – $25''$  across, with a mean flux density of  $\sim 2.8 \text{ mJy}$  per  $1''.39 \times 0''.6$  beam at 1.5 GHz. The base narrows as it extends to the NE, with a PA of  $\sim 50^\circ$ . A schematic diagram of these features is shown in Figure 6(c). The tower is terminated by two bow-shock-like structures. Grayscale contours of these are displayed in Figure 7(a).

The second feature is the polarized source P1 that was first identified at 8 GHz (Yusef-Zadeh et al. 2012). At 1.5 GHz, P1 is resolved into two linear structures (see the total intensity image in Figure 6(b)), that appears to cross each other at right angles. One of the linear features has a PA  $\sim 50^\circ$ , as shown in Figure 7(b). Lastly, the region surrounding the polarized source P4 (Yusef-Zadeh et al. 2012) is shown at 1.5 GHz in Figure 7(c). This elongated feature extends for  $20''$  at 1.5 GHz with a PA of  $\sim 50^\circ$ . A number of blob-like structures were previously reported to the NE of this feature (Yusef-Zadeh et al. 2012).

## 3.3. Other Features

### 3.3.1. A Semi-linear Feature

We identify a striking semi-linear radio continuum feature projected perpendicular to the radio Sgr A\* ridge.<sup>10</sup> Figure 8(a)

<sup>10</sup> The Sgr A\* radio ridge should be distinguished from the mid-IR Sgr A\* ridge discussed by Schödel et al. (2011).

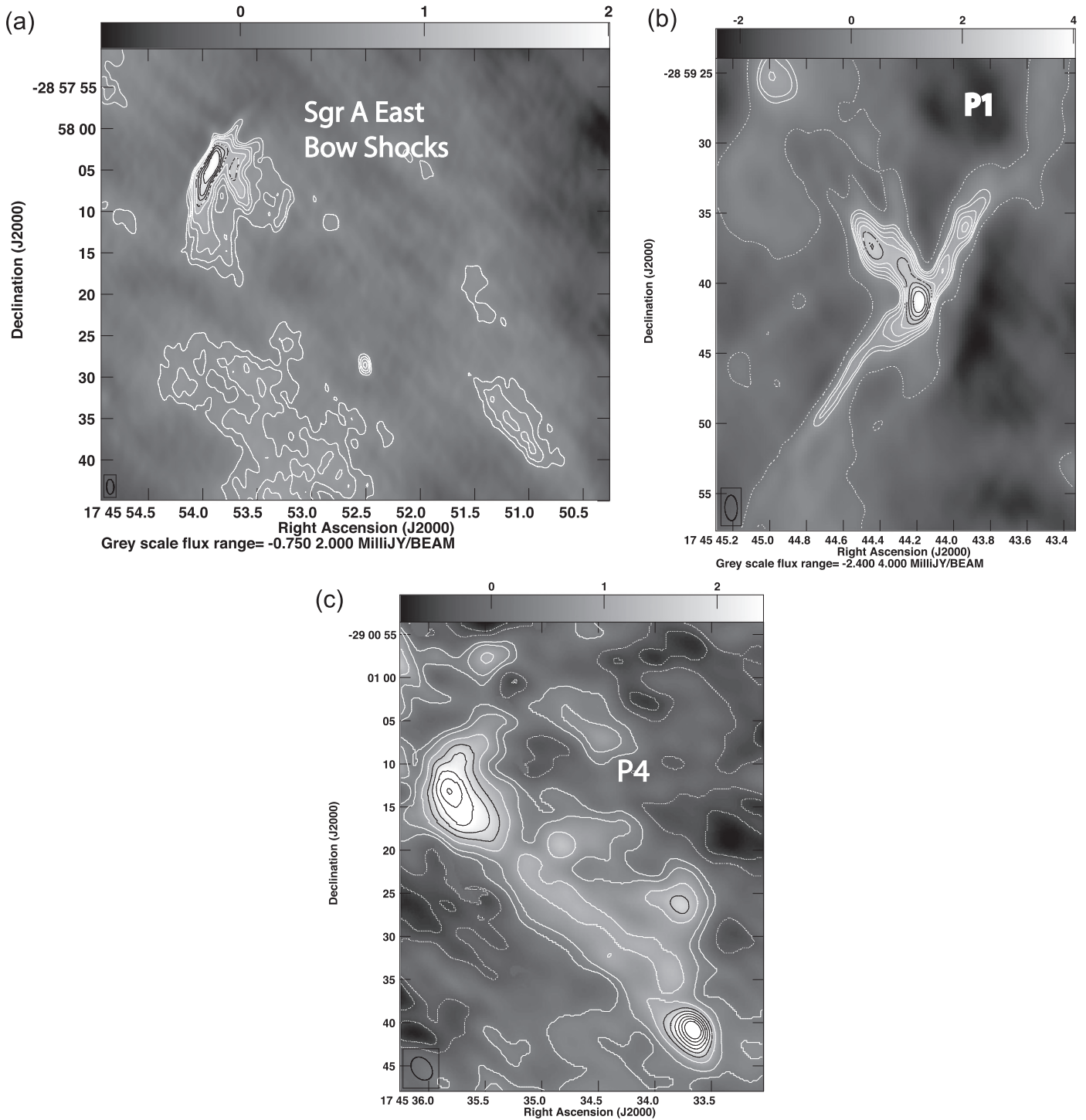


**Figure 7.** ((a)—Top left) grayscale contours of the bow shock region where the Sgr A East tower terminates at 1.52 GHz with a resolution of  $1''.81 \times 0''.89$  ( $PA = 1^\circ 65'$ ). The levels are set at  $-0.9, 0.4, 0.5, 0.6, 0.7, 0.9, 1.1, 1.3, 1.5, \& 1.7$  mJy beam $^{-1}$ . ((b)—Top right) similar to (a) except that the grayscale contours of P1— $0.5, 0.5, 0.7, 1, 1.3, 1.6, 2.0, 2.5, 3.0$  &  $3.5$  mJy beam $^{-1}$ . ((c)—Bottom) the P4 region at 1.52 GHz with a resolution of  $2''.9 \times 2''.2$  ( $PA = -38^\circ$ ). The grayscale range is between  $-0.8$  and  $2.4$  mJy beam $^{-1}$ . Contour levels are set at  $(-1, -0.5, 1, 2, \dots, 8) \times 0.5$  mJy beam $^{-1}$ .

shows a 5.5 GHz image that reveals roughly uniform brightness  $\sim 0.5$  mJy per  $0''.5 \times 0''.27$  beam. The semi-linear feature appears to arise from the ionized bar as it curves concave toward Sgr A\*, crosses the ridge at an angular distance of  $\sim 1''$  west of Sgr A\*, and continues to the north of Sgr A\*. To highlight this structure, white dashed lines are drawn along this radio feature. The semi-linear continuous structure has an

extent of  $5''$  and a width of  $0''.5$ , becoming wider and more diffuse as it extends to the north of Sgr A\*. The northern arm shows a discontinuity, as it approaches Sgr A\*, which is best seen at  $\alpha, \delta$  (J2000) =  $17^h 45^m 40^s.18, -29^\circ 0' 29''$  in Figures 1(a)–(c). The elongated features make a  $90^\circ$  change to the south in its direction as it approaches Sgr A\* (see the schematic diagram in Figure 9). The kinematics of ionized gas

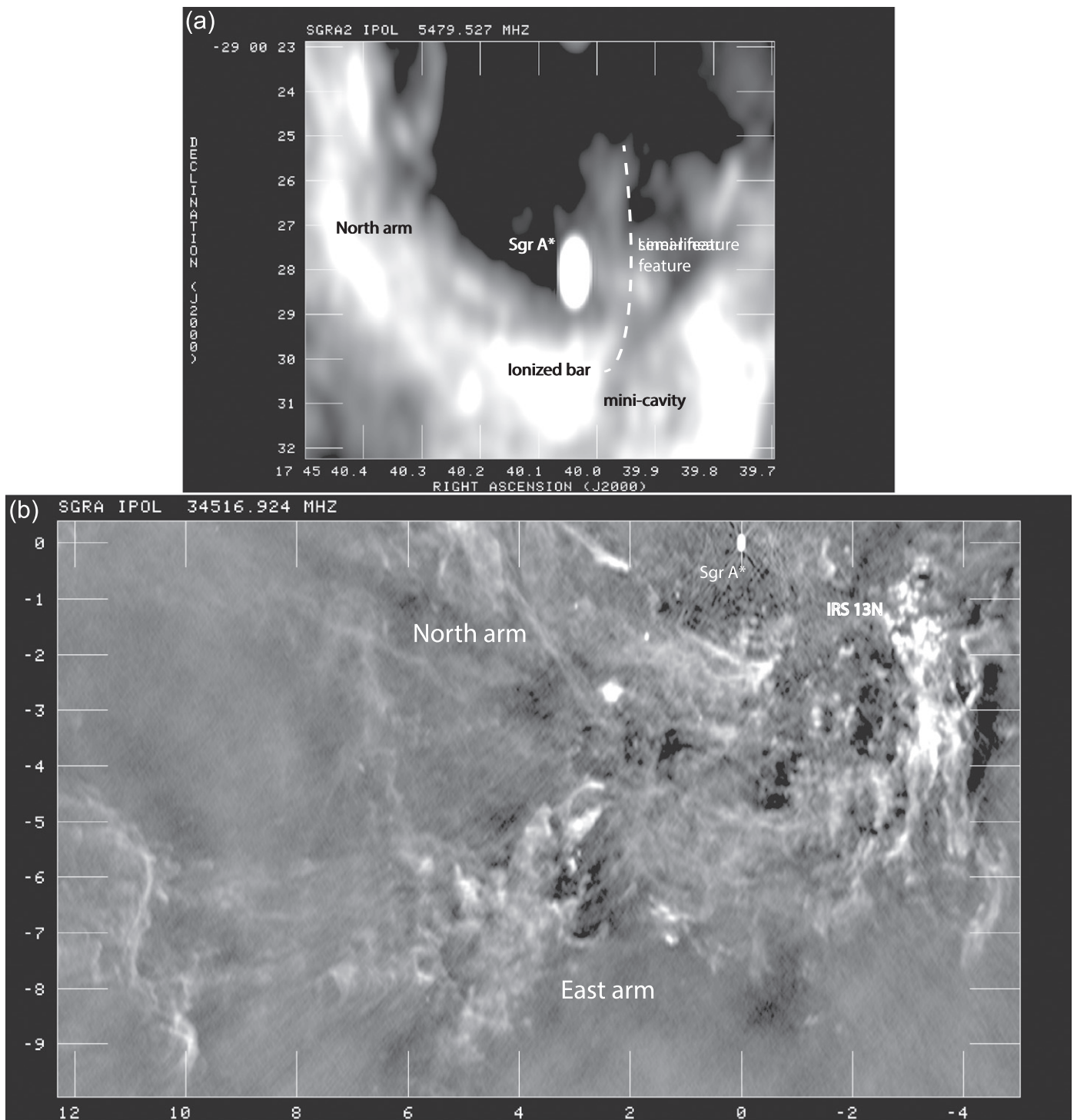


**Figure 8.** (a) The same as (b) except at 5.8 GHz, with a resolution of  $0''.59 \times 0''.27$ . (b) A grayscale 34 GHz continuum image of ionized gas showing the east and north arms of Sgr A West. The spatial resolution of this image is  $88.6 \times 46.5$  mas (PA =  $-1^\circ56$ ). Axes are in the direction of R.A. and decl. and the coordinates are given in arcseconds with respect to Sgr A\*.

show that the radial velocity of this elongated feature is close to zero  $\text{km s}^{-1}$  but changes by  $\sim 200 \text{ km s}^{-1}$  close to the location of the discontinuity (Zhao et al. 2009).

### 3.3.2. The Minicavity and the Bar

The bar of ionized gas lies a few arcseconds to the south of Sgr A\* where the eastern and northern arms of Sgr A West cross each other. High spatial resolution images of the ionized

bar show a minicavity of ionized gas with high velocity dispersion (Lacy et al. 1991; Roberts et al. 1996; Zhao et al. 2009). Figure 8(b) shows a larger area of the eastern arm and the minicavity at 34 GHz. The mini-cavity and the eastern arm are distinct from the north arm. High resolution observations have shown that the minicavity extends further to the SE (Zhao et al. 1991). The new images show that a gap separates the eastern and western halves of the minicavity and that the north and east arms are two distinct features associated with the

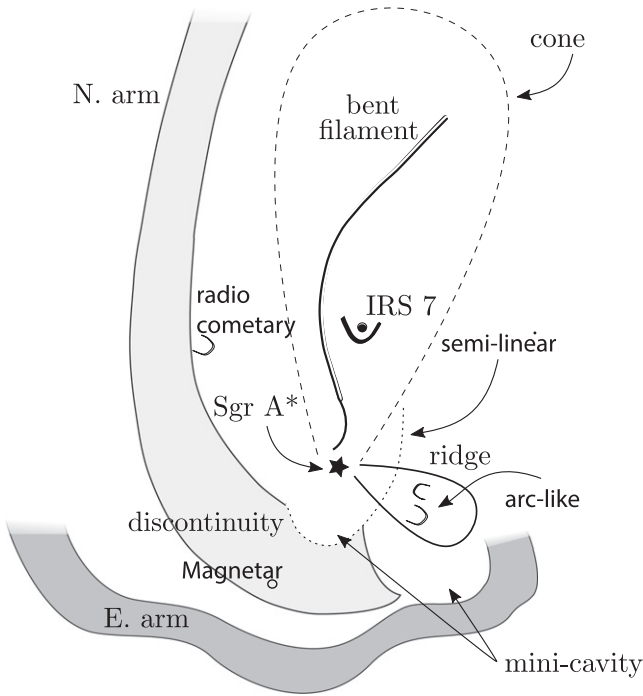


**Figure 9.** A diagram of prominent features in Sgr A West within  $50''$  of Sgr A\*.

eastern and western halves of the mini-cavity, respectively. The structure of the eastern arm has a wavy appearance with a wavelength of  $2''$ – $4''$  as it extends along the western half of the minicavity. Figure 9 shows a schematic diagram of the small and large-scale features revealed in the inner  $50''$  of Sgr A\*.

### 3.3.3. A Bent Filament

Figures 10(a) and (b) show the large-scale area at 1.5 and 5.5 GHz, respectively. A striking filamentary structure is seen within a cavity of ionized gas to the north of Sgr A\*. This bent and narrow filament resembles the nonthermal radio filaments seen throughout the Galactic center (e.g., Nord et al. 2004; Yusef-Zadeh et al. 2004). The southern end of this filament is pointed toward Sgr A\*. Figures 10(c) and (d) show the details of the bent filament at 1.5 GHz at two different resolutions, indicating that the filament may experience another bend at  $\sim 2''$  to the N of Sgr A\*. Because of the large angular size of Sgr A\* induced by scatter broadening at 1.5 GHz, it is not clear if there is an additional change in the PA of the bent filament in the inner  $1''$  of Sgr A\*. Figure 10(e) shows grayscale contours of 8.9 GHz emission from the filament. The surface brightness of the filament at 1.5 GHz is  $\sim 3$  mJy beam $^{-1}$  as it bends to the NW (see Figure 10). The length of this filament at 1.5 GHz is  $\sim 25''$ . The width of the filament is unresolved at 1.5 GHz but is partially resolved at roughly  $0''.3$  at 8.9 GHz. The cavity in which this bent filament lies, as best revealed in Figure 10(c), is dark and devoid of diffuse ionized gas at 1.5 GHz. This cavity has a cone-shaped structure and the cometary supergiant star IRS 7 (Rieke & Rieke 1989; Yusef-Zadeh et al. 1989; Serabyn et al. 1991; Yusef-Zadeh & Melia 1992) is seen within the cone structure at 5.5 GHz.

The bent filament lies in a region with varying background emission, thus accurate determination of the spectral index is not possible. Approximately accounting for the background flux, the surface brightness is  $\sim 3$ – $4$  mJy beam $^{-1}$  at 5.5 and

1.5 GHz, implying a flat spectrum between these frequencies. The sensitivity at 34 and 44 GHz is not sufficient to detect the bent filament. The origin of the bent filament is unknown, though its morphology gives the best jet-like appearance that may be originated within  $1''$  of Sgr A\*. It is also possible that this filament is a member of the population of nonthermal radio filaments found in the Galactic center, such as the linear filaments found within the inner few arcminutes of Sgr A\* where the Sgr A East SNR lies (Nord et al. 2004; Yusef-Zadeh et al. 2004). Future high resolution measurements at low frequencies, including proper motion observations, are required to constrain the nature of this bent structure.

## 4. DISCUSSION

Here we discuss four aspects of the new structures found near Sgr A\*. First, we interpret the arc-like sources in terms of recent low-mass star formation activity within  $2''$  of Sgr A\*. Second, we explain the origin of hot X-ray gas within the S-cluster as arising from colliding winds from mass-losing stars, either from low-mass young stellar objects (YSOs) or young B stars in the S-cluster or both, and estimate the accretion rate onto Sgr A\*. Third, we argue that the cometary radio structures and the Sgr A East tower are signatures of an interaction between a collimated outflow from Sgr A\* with a PA  $\sim 50^\circ$ – $60^\circ$  with the stellar envelopes and ionized gas along the path of the jet. The consequence of this interaction infers not only the mass loss rate from Sgr A\* but also provides a lower bound on the accretion rate onto Sgr A\*. Fourth, the ridge of radio emission is interpreted as due to past flaring activity associated with Sgr A\*.

### 4.1. Proplyd Candidates Near Sgr A\*?

The nature of the radio sources within two arcseconds of Sgr A\* is not clear. Two arc-like radio sources RS5 and RS6 resemble the bow-shock sources found at 34 GHz about  $20''$  away from Sgr A\* (Yusef-Zadeh et al. 2015b). As displayed in Figures 4(b), (c), RS5 and RS6 have near-IR counterparts. Although there is an early-type star, S1-22, that may be associated with RS6, RS5 is not identified as a near-IR star in various catalogs (e.g., Lu et al. 2009, 2013). There is no evidence for a known young and massive star associated with RS5. RS5 has 3.8 and  $2.18 \mu\text{m}$  counterparts, suggesting the dust, traced by near-IR emission, and ionized gas, as traced at radio, are either intermixed, or else closely related though separate, as observed in photodissociating regions. Because of the strong radiation field that produces high temperature of the ionized gas, as traced by radio emission, dust grains mixed in with ionized gas would have been evaporated. Thus, RS5 resembles the population of bow-shock sources that have recently been found  $20''$  from Sgr A\* and are interpreted as candidate photoevaporative protoplanetary disks (proplyds) associated with newly formed low-mass stars (Yusef-Zadeh et al. 2015b). The short expansion timescale and the low density of ionized gas associated with the arc-like structures provide strong arguments in favor of protoplanetary disks (Li & Loeb 2013; Yusef-Zadeh et al. 2015b).

To examine the protoplanetary disk scenario, we compared radio and near-IR flux from RS5 and another proplyd candidate, the so-called P8 source (Figure 2(c) in Yusef-Zadeh et al. 2015b). P8 is among 44 proplyd candidates found within  $25''$  of Sgr A\*. Figures 11(a) and (b) show a horizontal slice

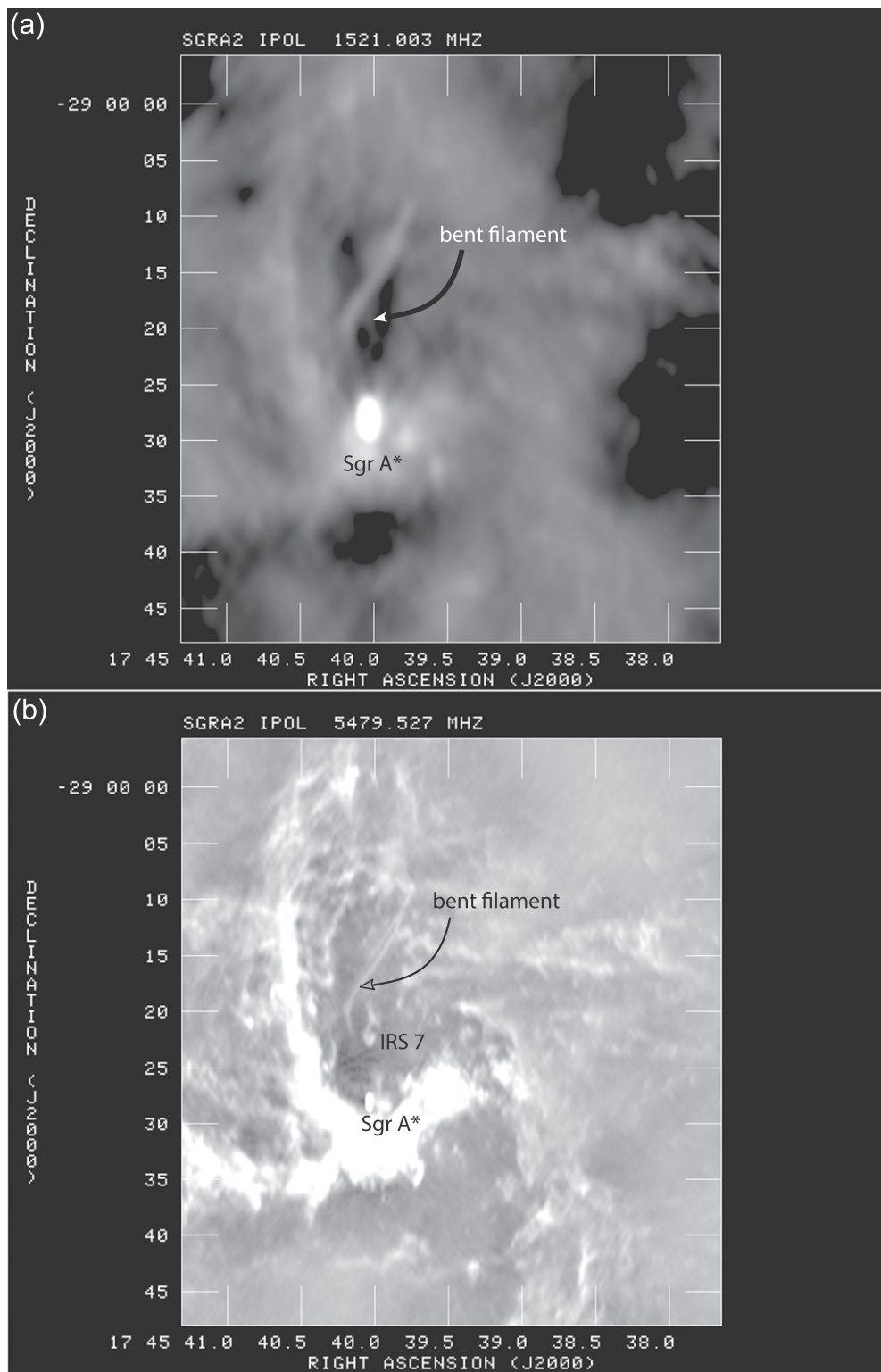


**Figure 10.** (a) A 1.5 GHz continuum image with a resolution of  $1''.87 \times 0''.9$  ( $PA = 0^\circ$ ) shows Sgr A West and a striking filamentary structure adjacent to the north arm. (b) Similar to (a) except at 5.5 GHz with a spatial resolution of  $0''.59 \times 0''.27$ . (c) A 1.5 GHz image of the bent filament and Sgr A\* with a resolution of  $1''.8 \times 0''.9$  ( $PA1^\circ$ ). Sgr A\* is marked with a star. (d) Similar to (c) except with a resolution of  $1''.4 \times 0''.6$  ( $PA1^\circ$ ). (e) Contours of 8.9 GHz emission from the bent filament with a resolution of  $0''.34 \times 0''.19$  are set at  $(-0.05, 0.05, 0.1, 0.2, \dots, 0.7, 1, 1.5, 2) \times 0.5$  mJy beam $^{-1}$ .

that crosses RS5 and P8, respectively, at 35 GHz, and the L' and K<sub>s</sub> near-IR bands. The arrows point to the location of proplyd candidates. The emission from RS5 in the three panels lies at pixel 25.29, with a peak surface brightness of 0.31 mJy beam $^{-1}$  (beam =  $88 \times 45$  mas $^2$ ), 49 mJy pixel $^{-2}$  (pixel

size = 27 mas) and 1.5 mJy pixel $^{-2}$  (pixel size = 27 mas) at 35 GHz, L', and K<sub>s</sub>, respectively. Similarly, the intensity profile of P8 is shown in Figure 11(b) with a low signal-to-noise emission at the K<sub>s</sub> band. The arc-like sources are likely photoionized externally by the UV radiation field from the

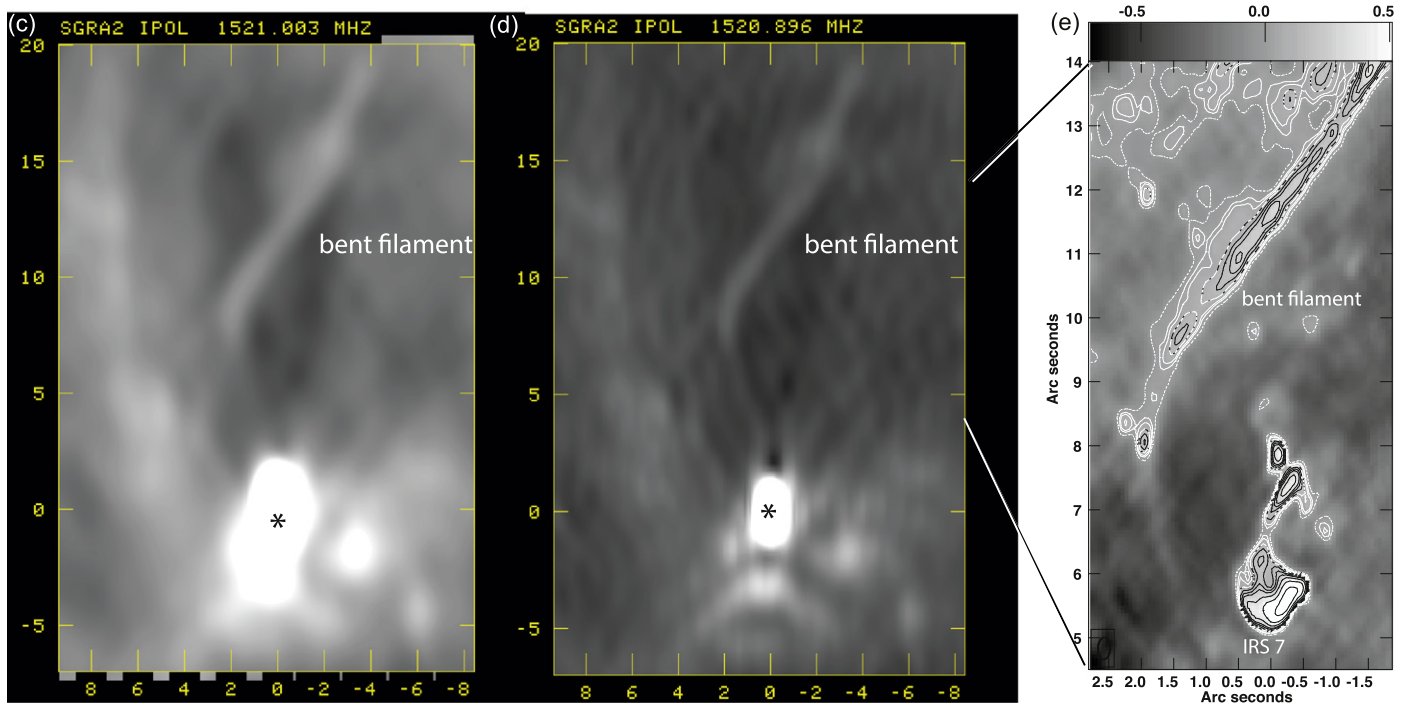


Figure 10. (Continued.)

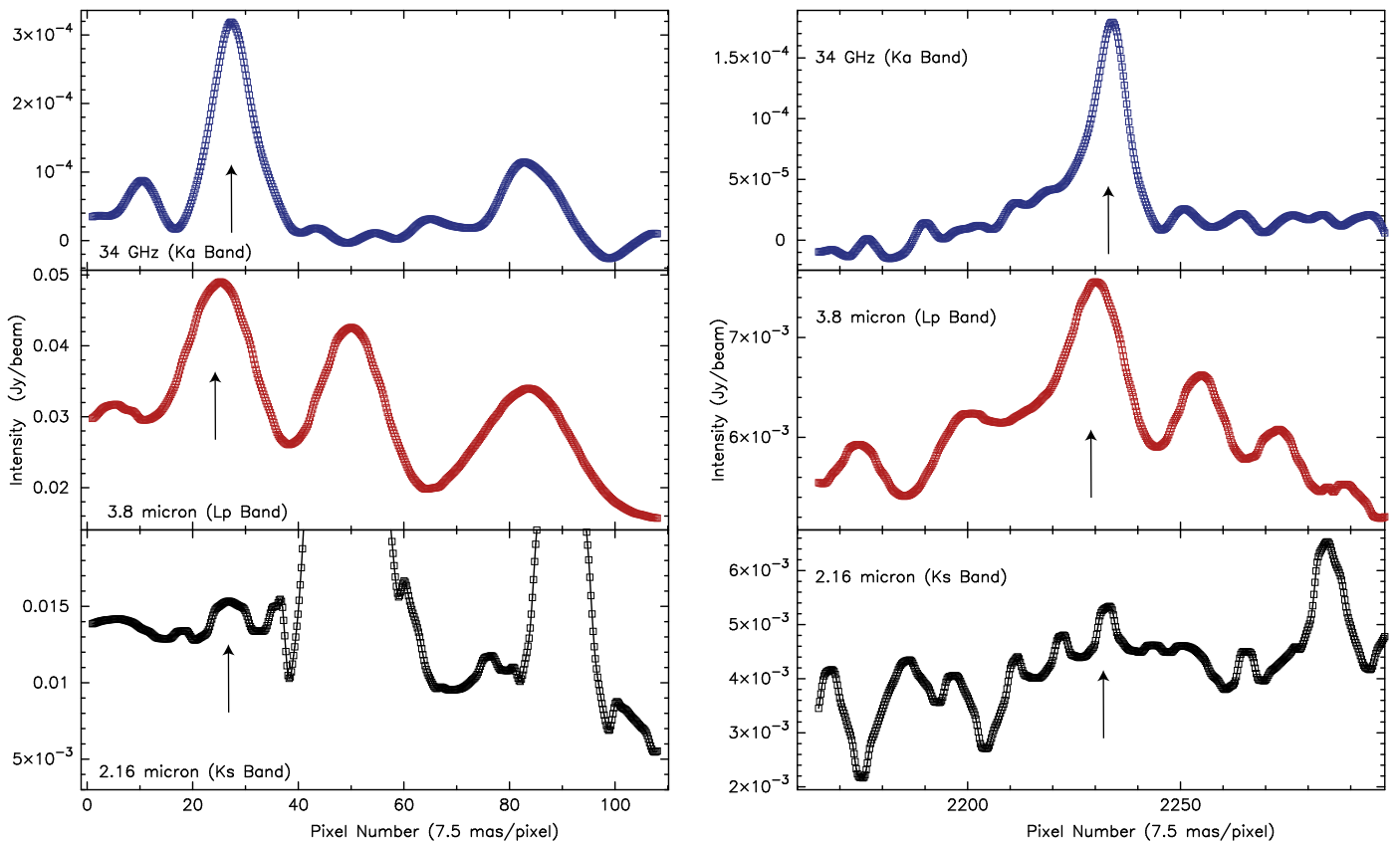
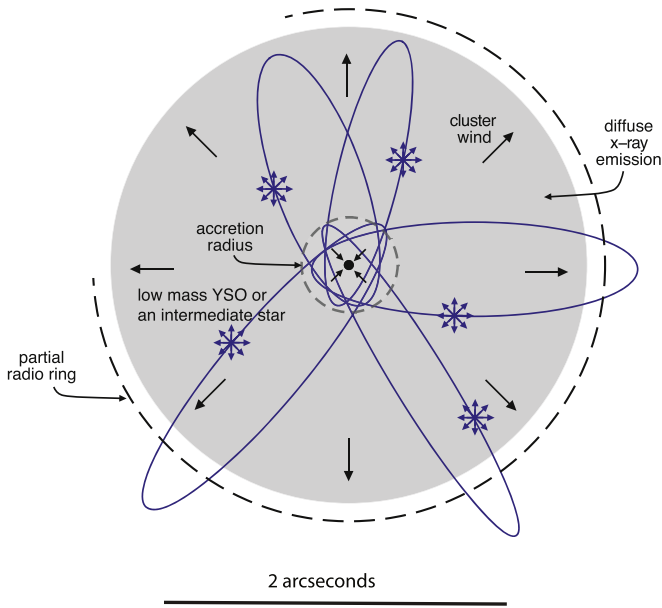


Figure 11. Three panels showing the flux density of RS5 (left) and P8 (right) as a function of the pixel number based on three different registered images at 34 GHz, 3.8  $\mu\text{m}$ , and 2.16  $\mu\text{m}$ . The slice for RS5 was made at a constant declination  $-29^{\circ}00' 28''.25$  between  $17^{\text{h}}45^{\text{m}}39^{\text{s}}.879$  and  $17^{\text{h}}45^{\text{m}}39^{\text{s}}.940$  for an extent of  $\sim 0''.81$ .

$\sim 100$  OB and WR stars that lie within  $10''$  of Sgr A\*. We suggest that RS5 and P8 are protoplanetary candidates that are externally photoionized by strong sources of UV radiation.

Assuming that radio emission traces the ionization front of protoplanetary candidates, we use the flux at L' and K<sub>s</sub> to determine the temperature of dust emission from the outer surface of a hot



**Figure 12.** A schematic diagram of a model of the emission within the inner  $1''$  of Sgr A\* where the S-cluster is located. The diffuse X-ray cluster wind is produced from merged winds of mass-losing B stars or material photoevaporating from the disks of young low mass stars that orbit Sgr A\*. The X-ray cluster wind plays two roles. First, its pressure is sufficient to prevent external material beyond  $1''$  of Sgr A\* to approach Sgr A\*. Second, the inner material feeds Sgr A\* (c.f. Loeb 2004; Quataert 2004).

disk. We use the measured fluxes at the  $K_s$  and  $L'$  bands to check that the emission is consistent with a protoplanetary disk irradiated by the intense radiation field in the inner Galaxy. The flux at frequency  $\nu$  is given by

$$S_\nu = B_\nu(T_d)(1 - e^{-\tau_\nu})\Omega, \quad (1)$$

where  $T_d$  is the dust temperature and  $\tau_\lambda = 6 \times 10^{-27} N_H/\lambda$   $\text{H cm}^{-3}$  is the optical depth (Draine & Lee 1984) and  $\Omega$  is the solid angle of the source. Given  $\Omega$ , the observed fluxes in the two bands determine the dust temperature  $T_d$  and associated hydrogen column  $N_H$ .

For RS5 we obtain extinguished  $K_s$  and  $L'$  band fluxes of 1.5 mJy and 25 mJy, respectively. Infrared emission from RS5 traces dust emission from the protoplanetary disk candidate. The infrared emission is unresolved at the  $K_s$  band, implying that the solid angle is less than  $(27 \text{ mas})^2$ , equivalent to radius  $R \lesssim 110 \text{ AU}$  at 8 kpc. Adopting 3 mag of extinction in  $K_s$  band and noting that  $A_\lambda \propto 1/\lambda$ , Equation (1) yields the extinction corrected  $K_s$  and  $L'$  fluxes for a dust temperature of 740 K in a layer at the disk surface with  $N_H \approx 1.5 \times 10^{20} \text{ cm}^{-2} (R/100 \text{ AU})^{-2}$ . These values are reasonable provided that the external radiation field is strong enough. To check this, we note that the bolometric luminosity estimated from the  $3.8 \mu\text{m}$  flux is  $4\pi d^2 \nu S_\nu \approx 200 L_\odot$ . Adopting a total luminosity  $L_* \approx 2 \times 10^7 L_\odot$  in the inner 0.1 pc due to the population of hot stars surrounding Sgr A\*, implies then the disk intercepts  $\sim L_*/(4\pi(0.1 \text{ pc})^2) \times 2\pi R^2 \sim 240(R/100 \text{ AU})^2 L_\odot$ , suggesting that  $R \sim 100 \text{ AU}$ . Source P8 is less constrained, with an extinguished  $L'$  band flux of 1.8 mJy, and a  $K_s$  band upper limit of 0.5 mJy. This yields an upper limit on the dust temperature of 1250 K. The high dust temperatures associated with RS5 and P8 imply that these ionized features are associated with a layer of hot dust and that they are not blobs of ionized gas. The luminosity and column density of gas estimated from near-IR

data here are very similar to those made toward proplyds found in Orion (Shuping et al. 2006). The EUV Lyman continuum ionization radiation from a smaller number of massive stars is estimated to be  $\Phi \approx 8 \times 10^{49} \text{ s}^{-1}$  (Genzel et al. 1994) and for an assumed  $\sim 0.5 \text{ pc}$  distance from the source of ionization, the incident ionizing photon flux is  $\Phi/(4\pi(0.5 \text{ pc})^2) \approx 2 \times 10^{12} \text{ s}^{-1} \text{ cm}^{-2}$ . We also note that the peak flux densities of radio source RS5 are roughly five times stronger than those of distant proplyd candidates (P8 and P26 in Yusef-Zadeh et al. 2015b), consistent with the suggestion that RS5 is photoionized by the stellar cluster near Sgr A\*.

Another possibility is that these bowshock structures are blobs of ionized gas and hot dust that orbit around Sgr A\* and have a short photoevaporative lifetime. As discussed by Yusef-Zadeh et al. (2015b) the photoevaporation timescale is  $\approx 300 \text{ yr}$ , unless there is a reservoir of neutral material associated with a low-mass star. In addition, the dusty blob must be bound by self-gravity to avoid tidal disruption by Sgr A\*. A distance of 0.1 pc from Sgr A\*, the density of the blob must exceed  $n_H \gtrsim 10^{11} \text{ cm}^{-3}$  with a  $M \approx 0.5 r_{100} M_\odot$ . These values are sufficient for the collapse and formation of stars. To support our argument, we note that the G2 source was considered to be a cloud of dust and gas orbiting Sgr A\* (Gillessen et al. 2012). However, recent measurements suggest that G2 is unlikely to be an isolated cloud of gas and must have an embedded core, possibly a pre-main sequence star (Scoville & Burkert 2013; Witzel et al. 2014). Future submillimeter observations should test this scenario by searching for emission from cool dust in the inner disks of the proplyd candidates.

#### 4.2. Stellar Mass Loss and the Hot Gas Associated with Sgr A\*

To first order, the diffuse X-ray emission centered on Sgr A\* is fit by an optically thin thermal plasma with  $kT = 3.5 \text{ keV}$ , total X-ray luminosity in the 2–10 keV band  $\sim 3 \times 10^{33} \text{ erg s}^{-1}$ , and mass  $\sim 1 \times 10^{-3} M_\odot$  (Baganoff et al. 2003; Wang et al. 2013), implying a mean number density  $n_H \approx 140 \text{ cm}^{-3}$ . This material is usually presumed to be accreting onto Sgr A\*, and there is indeed evidence for an associated non-thermal component arising from the gas falling in toward Sgr A\* (Wang et al. 2013). The Bondi accretion rate onto Sgr A\* is  $\sim 10^{-5} M_\odot \text{ yr}^{-1}$ , but this is likely an overestimate given that Sgr A\* is not embedded in a uniform zero angular momentum medium. Sub-millimeter polarization measurements indicate that the accretion rate close to the event horizon is  $\sim 10^{-7} - 10^{-9} M_\odot \text{ yr}^{-1}$ , depending on assumptions about the magnetic field (Marrone et al. 2007).

This gas is generally thought to be supplied by the combined winds of the mass-losing young stars in the central parsec of the Galaxy, which are estimated to supply material to Sgr A\* at a rate of a few times  $10^{-6} M_\odot \text{ yr}^{-1}$  (Coker & Melia 1997; Rockefeller et al. 2004; Cuadra et al. 2006, 2008). However, the discovery of populations of young stars within the S-cluster which consists of  $\sim 16$  B dwarfs and 3 O stars on highly eccentric orbits within  $1''$ , begs the question whether mass loss from these stars plays a dominant role in supplying gas to the vicinity of Sgr A\*. Loeb (2004) suggested that mass loss from the S-stars could explain this hot gas. In this picture winds from the stars are shocked to high temperature because of the high orbital speeds of the S-stars. Attaining a shock temperature of 3.5 keV requires a shock speed  $\sim 1700 \text{ km s}^{-1}$ , which corresponds to the Keplerian speed at 6 mpc ( $0''.15$ ) from Sgr A\*. Loeb (2004) suggested that the S-stars were OB or WR stars

with powerful winds, but it is now known that they are mainly B stars. Theoretical calculations suggest that B stars have individual mass loss rates  $\lesssim 10^{-8} M_{\odot} \text{ yr}^{-1}$  (e.g., Vink et al. 2000; Puls et al. 2008), insufficient to replenish the hot gas. However, the mass loss rates are known to be severely underpredicted, and recent modeling of the shells blown in molecular clouds by young A and B stars suggests far higher rates,  $\sim 10^{-7} - 10^{-6} M_{\odot} \text{ yr}^{-1}$  (Offner & Arce 2015). Thus follows the suggestion that the wind created by the merging of individual stellar winds from the B stars in the S-star cluster expands and excludes the shocked winds from O and WR stars in the central parsec of the Galaxy (c.f. Loeb 2004).

The increasing evidence for YSOs within arcseconds of Sgr A\*, such as the sources RS5 and P8 as discussed in this paper, suggests that YSOs may be intermingled with the disk and S-star populations. As pointed out earlier, the so-called G2 cloud could be another low-mass YSO candidate orbiting Sgr A\* (Scoville & Burkert 2013).

The young, massive stars within  $\sim 0.05 - 0.5$  pc of Sgr A\*, a fraction of which are found on the so-called clockwise rotating disk, are formed between 2.5 and 6 Myrs ago (Lu et al. 2009). Thus, it is reasonable to assume that a population of lower mass stars, with attendant protoplanetary disks, is also present. The IMF is not as top-heavy as originally thought, but still somewhat flatter than the Salpeter or Kroupa IMFs, with  $\phi(M) \propto M^{-1.75}$  (Lu et al. 2013). Of the 31  $K_s \leq 16$  mag stars that reside within the projected distance of  $1''$  from Sgr A\*, 16 are B stars, 3 are O stars, and 12 are late-type stars, of which 16 B stars and 3 late type stars are likely to be true members after correcting for contamination by foreground and background stars (Genzel et al. 2010). Extrapolation down to solar-mass stars is fraught with uncertainty but assuming that there are  $\sim 16$  young stars within the S-cluster with masses exceeding  $3.5 M_{\odot}$  implies about 120 stars with masses between 0.5 and  $3.5 M_{\odot}$ . If these stars, which presumably have ages  $\sim 3 \times 10^6$  years, still possess disks, then are exposed to the intense radiation from the OB stars in the central 0.5 pc ( $G_0 \sim 10^5$ ) they will collectively lose mass by photoevaporation at a rate  $\sim 10^{-6} M_{\odot} \text{ yr}^{-1}$ . In addition, material mass will be tidally stripped from these disks. Here, we assumed that B-type main sequence stars are formed at the same time as the population of OB and WR stars beyond the inner  $1''$  of Sgr A\*. The truncation radius for stellar mass  $M$  is  $r_t \approx (2M_*/M_{\text{BH}})^{1/3} r \approx 8 \text{ AU} (M/M_{\odot})^{1/3} (r/5 \text{ mpc})$ , where  $r$  is the distance from Sgr A\*. Figure 12 shows a schematic diagram of how low mass stars feed Sgr A\* as well as create a high pressure X-ray gas that prevents the material belonging to the inner 0.5 pc to fall into Sgr A\*.

The X-ray emission extends slightly beyond the S-cluster boundary, suggesting that the gas is not bound to Sgr A\* and instead escapes as a supersonic wind (cf. Quataert 2004). At some point the escaping cluster wind encounters the material supplied by the combined winds of the massive young stars beyond 0.5 pc. In our proposed scenario, the outflowing material from the S-cluster prevents this material from reaching within  $1'' - 2''$  of Sgr A\*. Our interpretation of the diffuse X-ray emission associated with Sgr A\*, due to an expanding hot wind fed by the S-cluster (whether B stars or low-mass YSOs or both), yields a very different estimate of the accretion rate onto Sgr A\* than the standard picture. Instead, a small fraction of the stellar winds injected very close to Sgr A\* is captured by the black hole; a rough estimate of the accretion rate is obtained by

using the Bondi–Hoyle accretion rate appropriate for a medium of density  $\rho$  moving by a point mass  $M = 4 \times 10^6 M_{\odot}$  at the typical stellar orbital speed  $v = 4000 \text{ km s}^{-1}$ , i.e.,  $\dot{M} = 4\pi G^2 M^2 \rho / v^3 \approx 3 \times 10^{-7} M_{\odot} \text{ yr}^{-1}$ . This estimate is likely an upper limit because it neglects any net angular momentum. The proposed model naturally reduces the accretion rate to a level consistent with submillimeter rotation measure constraints, and removes the need for inflow–outflow solutions, which magically turn most of the inflowing material around at very small radii and eject it to infinity.

### 4.3. Jet Activity of Sgr A\*

A linear feature with an extent of  $\sim 3$  pc at a PA of  $\sim 60^\circ$  (Yusef-Zadeh et al. 2012) was recently suggested to be tracing a jet from Sgr A\* interacting with the surrounding medium. Here we describe two additional features, the Sgr A East tower and cometary sources, with PAs  $\sim 60^\circ$ . These features are suggestive of a jet interacting at sites near Sgr A\*.

#### 4.3.1. The Sgr A East Tower

We recently reported the tentative detection of a continuous linear structure symmetrically centered on Sgr A\* with PAs  $\sim 60^\circ$  and  $240^\circ$  (Yusef-Zadeh et al. 2012). The feature is terminated by linearly polarized structures P1 and P4  $\sim 75''$  from Sgr A\* at a PA  $\sim 60^\circ$  and  $240^\circ$ , respectively. This structure was interpreted as a mildly relativistic jet interacting with the ionized gas orbiting Sgr A\*. We observed a larger region around Sgr A\* and have identified additional sites of possible interaction between this jet candidate and the Sgr A East SNR. We presented the striking tower structure  $150''$  NE of Sgr A\*. This tower is an extension of the Sgr A East shell distorted toward the NE. We note multiple bow shock-like structures at the location where the tower terminates. In addition, structural details of P1 and P4 show linear structures that are aligned along the jet candidate. Altogether, morphological structures presented at radio support a picture in which a energetic jet-driven outflow is required to explain the distortion of the Sgr A East shell, as well as the alignment of a number of sources at PAs  $\sim 50^\circ - 60^\circ$  to the NE and PAs  $\sim 230^\circ - 240^\circ$  to the SW.

We adopt jet parameters  $\gamma \sim 3$ ,  $\dot{M} \sim 1 \times 10^{-7} M_{\odot} \text{ yr}^{-1}$ , and opening angle  $10^\circ$ . Then the jet pressure at the location of the tower,  $150''$  (or 6 pc) from Sgr A\*, is about  $P_{\text{jet}} = \dot{M} \gamma c / (4\pi d^2) \approx 4 \times 10^{-8} \text{ dyn cm}^{-2}$ . This is able to push through the thermal X-ray emitting gas filling the interior of Sgr A East at a speed  $\sqrt{P_{\text{jet}}/\rho} \approx 600 \text{ km s}^{-1}$ , implying a crossing time  $\sim 10^4$  years, assuming the tower is 6 pc away from Sgr A\*.

The jet is also able to drag a portion of the Sgr A East shell. The intensity of the synchrotron emission from the tower, i.e., 2.8 mJy per  $1''39 \times 0''6$  beam at 1.5 GHz, implies an equipartition field of 0.7 mG and a total pressure of  $2 \times B^2/8\pi \approx 3.5 \times 10^{-8} \text{ erg cm}^{-3}$  (Here we have adopted a source depth 1 pc, an  $E^{-2}$  electron spectrum extending between 1 MeV and 10 GeV, and assumed that the energy density in protons is 100 times that for the electrons). The jet pressure is comparable to the magnetic pressure in the nonthermal shell of Sgr A East, thus the jet is able to push through. This picture implies that Sgr A East lies close to Sgr A\*. The absorption of Sgr A West against Sgr A East (Yusef-Zadeh & Morris 1987; Pedlar et al. 1989) suggest that the NE

jet must be moving away from us to be interacting with the shell of Sgr A East.

An alternative possibility is that the tower is generated by the passage of a neutron star that received a large velocity kick at birth. The neutron star overtakes the remnant and produces a trail behind it as it interacts with the remnant. However, the trail behind the neutron star is expected to be narrow in this picture, unlike the observed structure of the extended base and the bow shock structures. Other SNRs also show jet-like or chimney-like structures at the edge of the remnant (e.g., Crab and CAS A), so it may be that the Sgr A East tower is produced in the remnant by a generic mechanism that is not associated with Sgr A\*.

#### 4.3.2. Cometary Sources

Radio and infrared images, as described above, indicate an alignment of a number of sources within a few arcseconds of Sgr A\* at a PA around  $50^\circ$ . These include the cometary structures X7 and X3 located SW, within  $0''.8$  and  $3''.4$  of Sgr A\*, respectively (Mužić et al. 2007, 2010). Both X3 and X7 show proper motions in the direction away from the direction toward Sgr A\*, suggesting that the bow-shock morphology of these sources is produced by an outflow from the direction of Sgr A\* and not by their motion (Mužić et al. 2007, 2010). We now detect two additional cometary sources F1 and F2, within  $4''.8$  NE of Sgr A\*. These sources lie within  $5''$  of Sgr A\* aligned at a PA  $\sim 50^\circ$ . Mužić et al. (2007, 2010) explain the origin of X3 and X7 in terms of an outflow either from the cluster wind interacting with the atmosphere of stars, or an outflow from Sgr A\* driving a shock that produces the cometary morphology. Given that almost all the cometary sources, X3, X7, source F1 (radio cometary), and F2 (MIR cometary), have the same PA as that of polarized sources P1 and P4 and the Sgr A East tower, a collimated outflow from Sgr A\* could be a better alternative to explain the origin of cometary structures.

The cometary sources are marginally resolved, implying stand-off distances equivalent to  $\sim 50$  mas at 8 kpc, i.e.,  $\sim 6 \times 10^{15}$  cm. The ionized gas mass derived from the 35 GHz flux density  $\sim 0.2$  mJy beam $^{-1}$  is  $\sim 4 \times 10^{-5} M_\odot$ , and adopting a wind speed of  $750$  km s $^{-1}$  we obtain mass loss rates  $\sim 10^{-5} M_\odot$  yr $^{-1}$  and ram pressures at the stand-of distance  $\sim 10^{-4}$  dyn cm $^{-2}$ . This is comparable to the jet ram pressure at  $\sim 0.1$  pc from Sgr A\* and compatible with the projected separations of X3, F1 and X7 sources, i.e., 0.13, 0.19, 0.03 pc.

#### 4.4. Flaring Activity of Sgr A\*

One possible explanation for the ridge of radio emission is related to the flaring activity of Sgr A\*. Past monitoring campaigns have found evidence for a time delay of  $\sim 30$  minutes between the peak emission at 43 and 22 GHz (Yusef-Zadeh et al. 2006, 2009; Brinkerink et al. 2015). This time delay is consistent with a picture in which an overpressured synchrotron emitting plasma blob at these wavelengths is initially optically thick. The blob then expands subrelativistically, peaks, and declines at each frequency once it becomes optically thin. In this picture, the blob-like and arc-like structures noted in the east–west ridge of emission detected at radio wavelengths are interpreted to be expanding blobs produced by flaring activity escaping from Sgr A\*. If the thermal density of expanding blobs is sufficient to overcome the external pressure, the outflow rate of thermal blobs of

plasma is estimated to be  $\lesssim 2 \times 10^{-8} M_\odot$  yr $^{-1}$  (Yusef-Zadeh et al. 2006). The expansion blob model has successfully been applied to flaring activity of microquasars where outflows have been detected (e.g., Fender & Belloni 2004).

Another possibility is that the ridge of radio emission results from the interaction of thermal winds from the cluster of young massive stars with the gravitational potential of Sgr A\*. Wardle & Yusef-Zadeh (1992) considered a picture in which the 16 IRS stars are the source of ionized winds interacting with Sgr A\*. In this picture, thermal winds are focused by Sgr A\* and form blobs of hot gas in the Sgr A\* ridge. Given that recent observations indicated that mass-losing stars are members of a cluster that lie in a disk orbiting Sgr A\*, it is not clear how the ridge is produced asymmetrically on one side of Sgr A\*.

VLBA measurements on a mas scale have identified elongated structure associated with Sgr A\* at 43 GHz with a PA of  $95^\circ$  (Bower et al. 2014). These authors explain this elongation in terms of both jet and accretion disk models. The radio plume and the ridge of emission closest to Sgr A\* in Figure 1(a) lie along a PA similar to the intrinsic elongation of Sgr A\*. This suggests that the elongation of Sgr A\* might be associated with blobs of radio emission detected within the ridge but on a scale roughly 2000 times smaller than the ridge of emission from Sgr A\*. The inference is that the radio sources in the plume-like and ridge structures are indirectly tracing the interaction of an outflow due to flaring activity of Sgr A\* and stars located in the S-cluster. The orientation of the outflow from flaring activity is not collimated by the disk so the opening angle could be large, as evidenced in the plume structure. On the other hand, the jet from Sgr A\* is presumably collimated by the disk and has a different PA than that of blobs of gas ejected from the corona of the accretion disk of Sgr A\* due to its flare activity.

#### 4.5. Conclusions

##### 4.5.1. Morphology

In summary, several new morphological features are revealed within the inner  $30''$  of Sgr A\*. On a scale of few arcseconds, an east–west plume-like ridge of emission appears to arise from Sgr A\* toward SW. This diffuse feature shows eight radio sources within  $2''$  of Sgr A\*, two of which are extended with arc-like morphology. One of the arc-like sources RS5 faces in the general direction of Sgr A\* whereas the other RS6 faces away from the direction of Sgr A\*. Although the ridge of emission is seen on one side of Sgr A\*, we also detect new cometary and head-tail structures (sources F1, F2, and F3) within  $13''$  of Sgr A\* to the NE at the PA of  $\sim 50^\circ$ – $60^\circ$ , pointing in the direction of Sgr A\*. Two previously identified cometary sources, X3 and X7, located  $3''$  and  $0''.7$  to the SW of Sgr A\*, respectively, we detected at a PA of  $\sim 50^\circ$ . These five cometary sources, X3, X7, and F1, F2, and F3 lie within  $\sim 5^\circ$  of a line passing through Sgr A\*. In addition, the ionized gas along the northern arm shows a discontinuity as the gas approaches Sgr A\*. The discontinuous structure is  $\sim 2''.5$  SE of Sgr A\*. We also note that some of the ionized gas from the northern arm shows a semi-linear feature curving around Sgr A\* and gives the appearance of a cloud leaving a trail of ionized gas along its path. On a scale of  $20''$ , we note a hollow cone-like structure, within which a striking bent filament is detected. On a scale of two arcminutes from Sgr A\*, we detect a new tower-like feature which appears to be associated with the Sgr A East shell. This remarkable structure becomes narrower as it extends to the NW

with a PA  $\sim 50^\circ$  and terminates with two bow-shock-like structures.

#### 4.5.2. Interpretation

The identification of new structural and kinematic features within a few arcseconds of Sgr A\* motivates a new scenario for the origin of the hot gas responsible for the diffuse X-ray emission associated with Sgr A\*. We argued for the presence of low-mass YSO candidates within the inner 2'' of Sgr A\* based on the morphology, size, and their dust and ionized properties. We also argued that the photoevaporation of low mass YSOs within the S-cluster and/or the ionized winds from the B-type main sequence stars merge to form a cluster wind that interacts with the surrounding orbiting ionized gas and excludes the combined winds from the massive stars in the central parsec of the Galaxy. The accretion rate of the S-cluster wind onto Sgr A\* is  $\lesssim 3 \times 10^{-7} M_\odot \text{ yr}^{-1}$ , helping to explain the low luminosity of Sgr A\*. This is an alternative to models in which the low luminosity is due to ejection of the bulk of the material accreted from larger radii. In our picture, the cluster wind accounts for the observed mass of X-ray gas within 1'' of Sgr A\* having a residence time of  $\sim 10^3$  yr. This X-ray gas plays two major roles. One is that the injected material during the cooling time of X-ray gas  $\sim 10^5$  yr expands away and leaves the inner 1'' of Sgr A\*. The injected ionized winds from the low-mass and/or young stars prevent the external material beyond 1'' from reaching Sgr A\*. The second role of the X-ray gas surrounding Sgr A\* is that a small fraction of the material that is initially injected by mass-losing stars finds its way to the black hole. It turns out that the accretion rate from the X-ray gas is lower than the the Bondi accretion rate of the same gas by two orders of magnitude. This is because the injected mass from stars has a much higher velocity near Sgr A\* and is highly stirred close to the black hole. Thus, a very small fraction of the X-ray gas accretes onto Sgr A\*. The accretion rate is consistent with submillimeter polarization measurements.

On a larger scale, we interpreted a number of cometary features and the distorted shape of the Sgr A East SNR in terms of the interaction of a collimated jet-driven outflow with the surrounding medium and impinging on stellar envelopes as well as a portion of the nonthermal Sgr A East shell. Lastly, we interpret that the east–west ridge of radio emission results from flaring activity of Sgr A\*. Flares are explained in terms of expanding, over-pressured plasma blobs that escape the gravitational potential of Sgr A\*. Unlike the jet-driven outflows, the outflowing material should not be highly collimated. Finally, we note that many of these suggestions can be tested by high-resolution proper motion and submillimeter measurements.

This work is partially supported by grants AST-0807400 and AST-1517246 from the NSF. The research leading to these results has also received funding from the European Research Council under the European Unions Seventh Framework Programme (FP/2007-2013)/ERC grant agreement No. 614922.

#### REFERENCES

- Baganoff, F. K., Maeda, Y., Morris, M., et al. 2003, *ApJ*, 591, 891  
 Baganoff, F. K., Bautz, M. W., Brandt, W. N., et al. 2001, *Natur*, 413, 45  
 Bower, G. C., Markoff, S., Brunthaler, A., et al. 2014, *ApJ*, 790, 1  
 Bower, G. C., Markoff, S., Dexter, J., et al. 2015, *ApJ*, 802, 69  
 Brinkerink, C. D., Falcke, H., Law, C. J., et al. 2015, *A&A*, 576, A41  
 Broderick, A. E., Fish, V. L., Doeleman, S. S., & Loeb, A. 2011, *ApJ*, 735, 110  
 Coker, R., & Melia, F. 1997, *ApJL*, 488, L149  
 Cuadra, J., Nayakshin, S., & Martins, F. 2008, *MNRAS*, 383, 458  
 Cuadra, J., Nayakshin, S., Springel, V., & Di Matteo, T. 2006, *MNRAS*, 366, 358  
 Draine, B. T., & Lee, H. M. 1984, *ApJ*, 285, 89  
 Eckart, A., Schödel, R., García-Marín, M., et al. 2008, *A&A*, 492, 337  
 Ekers, R. D., van Gorkom, J. H., Schwarz, U. J., & Goss, W. M. 1983, *A&A*, 122, 143  
 Falcke, H., & Markoff, S. 2000, *A&A*, 362, 113  
 Fender, R., & Belloni, T. 2004, *ARA&A*, 42, 317  
 Genzel, R., Eisenhauer, F., & Gillessen, S. 2010, *RvMP*, 82, 3121  
 Genzel, R., Hollenbach, D., & Townes, C. H. 1994, *RPPH*, 57, 417  
 Genzel, R., Schödel, R., Ott, T., et al. 2003, *ApJ*, 599, 812  
 Ghez, A. M., Salim, S., Weinberg, N. N., et al. 2008, *ApJ*, 689, 1044  
 Gillessen, S., Eisenhauer, F., Quataert, E., et al. 2006, *ApJL*, 640, L163  
 Gillessen, S., Eisenhauer, F., Trippe, S., et al. 2009, *ApJ*, 692, 1075  
 Gillessen, S., Genzel, R., Fritz, T. K., et al. 2012, *Natur*, 481, 51  
 Koyama, K., Hyodo, Y., Inui, T., et al. 2007, *PASJ*, 59, 245  
 Lacy, J. H., Achtermann, J. M., & Serabyn, E. 1991, *ApJL*, 380, L71  
 Li, G., & Loeb, A. 2013, *MNRAS*, 429, 3040  
 Li, Z., Morris, M. R., & Baganoff, F. K. 2013, *ApJ*, 779, 154  
 Loeb, A. 2004, *MNRAS*, 350, 725  
 Lu, J. R., Do, T., Ghez, A. M., et al. 2013, *ApJ*, 764, 155  
 Lu, J. R., Ghez, A. M., Hornstein, S. D., et al. 2009, *ApJ*, 690, 1463  
 Maeda, Y., Baganoff, F. K., Feigelson, E. D., et al. 2002, *ApJ*, 570, 671  
 Markoff, S., Bower, G., & Falcke, H. 2007, *MNRAS*, 379, 1519  
 Marrone, D. P., Baganoff, F. K., Morris, M. R., et al. 2008, *ApJ*, 682, 373  
 Marrone, D. P., Moran, J. M., Zhao, J. H., & Rao, R. 2007, *ApJL*, 654, L57  
 Moscibrokzka, M., et al. 2009, *ApJ*, 706, 497  
 Muno, M. P., Baganoff, F. K., Brandt, et al. 2008, *ApJ*, 673, 251  
 Mužić, K., Eckart, A., Schödel, R., Meyer, L., & Zensus, A. 2007, *A&A*, 469, 993  
 Mužić, K., Eckart, A., Schödel, R., et al. 2010, *A&A*, 521, A13  
 Nord, M. E., Lazio, T. J. W., Kassim, N. E., et al. 2004, *AJ*, 128, 1646  
 Offner, S. S. R., & Arce, H. G. 2015, *ApJ*, 811, 146  
 Panagia, N., & Felli, M. 1975, *A&A*, 39, 1  
 Park, S., Muno, M. P., Baganoff, F. K., et al. 2005, *ApJ*, 631, 964  
 Pedlar, A., Anantharamaiah, K. R., Ekers, R. D., et al. 1989, *ApJ*, 342, 769  
 Perger, M., Moutakka, J., Eckart, A., et al. 2008, *A&A*, 478, 127  
 Puls, J., Vink, J. S., & Najjarro, F. 2008, *A&ARv*, 16, 209  
 Quataert, E. 2004, *ApJ*, 613, 322  
 Reid, M. J., & Brunthaler, A. 2004, *ApJ*, 616, 872  
 Reid, M. J., Menten, K. M., Trippe, S., Ott, T., & Genzel, R. 2007, *ApJ*, 659, 378  
 Rieke, G. H., & Rieke, M. J. 1989, *ApJL*, 344, L5  
 Roberts, D. A., Yusef-Zadeh, F., & Goss, W. M. 1996, *ApJ*, 459, 627  
 Rockefeller, G., Fryer, C., Melia, F., & Warren, M. S. 2004, *ApJ*, 604, 662  
 Sanchez-Bermudez, J., Schödel, R., Alberdi, A., et al. 2014, *A&A*, 567, AA21  
 Schödel, R., Najjarro, F., Muzic, K., & Eckhart, A. 2010, *A&A*, 511, A18  
 Schödel, R., Merritt, D., & Eckart, A. 2009, *A&A*, 502, 91  
 Schödel, R., Morris, M. R., Muzic, K., et al. 2011, *A&A*, 532, A83  
 Schödel, R., Yelda, S., Ghez, A., et al. 2013, *MNRAS*, 429, 1367  
 Scoville, N., & Burkert, A. 2013, *ApJ*, 768, 108  
 Serabyn, Lacy, J. H., & Achtermann, J. M. 1991, *ApJ*, 378, 557  
 Shahzamanian, B., Eckart, A., Valencia-S., et al. 2015, *A&A*, 576, A20  
 Shcherbakov, R. V., & Baganoff, F. K. 2010, *ApJ*, 716, 504  
 Shuping, R. Y., Kassis, M., Morris, M., Smith, N., & Bally, J. 2006, *ApJL*, 644, L71  
 Tanner, A., Ghez, A. M., Morris, M. R., & Christou, J. C. 2005, *ApJ*, 624, 742  
 Vink, J. S., de Koter, A., & Lamers, H. J. G. L. M. 2000, *A&A*, 362, 295  
 Wang, Q. D., Nowak, M. A., Markoff, S. B., et al. 2013, *Sci*, 341, 981  
 Wardle, M., & Yusef-Zadeh, F. 1992, *Natur*, 357, 308  
 Witzel, G., Ghez, A. M., Morris, M. R., et al. 2014, *ApJL*, 796, L8  
 Yelda, S., Ghez, A. M., Lu, J. R., et al. 2014, *ApJ*, 783, 131  
 Yuan, F., Quataert, E., & Narayan, R. 2004, *ApJ*, 606, 894  
 Yusef-Zadeh, F., Arendt, R., Bushouse, H., et al. 2012, *ApJL*, 758, L11  
 Yusef-Zadeh, F., Bushouse, H., Schödel, R., et al. 2015a, *ApJ*, 809, 10  
 Yusef-Zadeh, F., Bushouse, H., Wardle, M., et al. 2009, *ApJ*, 706, 348  
 Yusef-Zadeh, F., Hewitt, J. W., & Cotton, W. 2004, *ApJS*, 155, 421  
 Yusef-Zadeh, F., & Melia, F. 1992, *ApJL*, 385, L41  
 Yusef-Zadeh, F., & Morris, M. 1987, *ApJ*, 320, 545  
 Yusef-Zadeh, F., Morris, M., & Ekers, R. 1989, in Proc. IAU 136, The Center of the Galaxy, ed. M. Morris (Dordrecht: Kluwer), 443  
 Yusef-Zadeh, F., Morris, M., & Ekers, R. D. 1990, *Natur*, 348, 45

- Yusef-Zadeh, F., Roberts, D., Wardle, M., Heinke, C. O., & Bower, G. C. 2006, *ApJ*, **650**, 189
- Yusef-Zadeh, F., Roberts, D. A., Bushouse, H., et al. 2014b, *ApJL*, **792**, L1
- Yusef-Zadeh, F., Roberts, D. A., Wardle, M., et al. 2015b, *ApJL*, **801**, L26
- Yusef-Zadeh, F., Wardle, M., Heinke, C., et al. 2008, *ApJ*, **682**, 361
- Yusef-Zadeh, F., Wardle, M., Roberts, D. A., et al. 2014a, in American Astronomical Society Meeting Abstracts 224, #213.01
- Yusef-Zadeh, F., Wardle, M., Sewilo, M., et al. 2015c, *ApJ*, **808**, 97
- Zamaninasab, M., Eckart, A., Dovčiak, M., et al. 2011, *MNRAS*, **413**, 322
- Zhao, J.-H., Goss, W. M., Lo, K. Y., & Ekers, R. D. 1991, *Natur*, **354**, 46
- Zhao, J.-H., Morris, M. R., & Goss, W. M. 2013, *ApJ*, **777**, 146
- Zhao, J.-H., Morris, M. R., Goss, W. M., & An, T. 2009, *ApJ*, **699**, 186